



1

2

3

4

5 The impact of Pacific Decadal Oscillation on springtime dust activity in Syria

6 Bing Pu<sup>1,2</sup> and Paul Ginoux<sup>1,2</sup>

7 <sup>1</sup>Atmospheric and Oceanic Sciences Program, Princeton University,

8 Princeton, New Jersey 08544

9 <sup>2</sup>NOAA Geophysical Fluid Dynamics Laboratory, Princeton, New Jersey 08540

10

11

12

13

14

15

16

17

18

19

20

21

22

23

24 Correspondence to: Bing Pu, Bing.Pu@noaa.gov



25 **Abstract.** The increasing trend of aerosol optical depth in the Middle East and a recent severe  
26 dust storm in Syria have raised questions as whether dust storms will increase and promoted  
27 investigations on the dust activities driven by the natural climate variability underlying the  
28 ongoing human perturbations such as the Syrian civil war. This study examined the influences of  
29 the Pacific decadal oscillation (PDO) on dust activities in Syria using an innovative dust optical  
30 depth (DOD) dataset derived from Moderate Resolution Imaging Spectroradiometer (MODIS)  
31 Deep Blue aerosol products. A significantly negative correlation is found between the Syrian  
32 DOD and the PDO in spring from 2003-2015. High DOD in spring is associated with lower  
33 geopotential height over the Middle East, Europe, and North Africa, accompanied by near  
34 surface anomalous westerly winds over the Mediterranean basin and southerly winds over the  
35 eastern Arabian Peninsula. These large-scale patterns promote the formation of the cyclones over  
36 the Middle East to trigger dust storms and also facilitate the transport of dust from North Africa,  
37 Iraq, and Saudi Arabian to Syria, where the transported dust dominates the seasonal mean DOD  
38 in spring. A negative PDO not only creates circulation anomalies favorable to high DOD in Syria  
39 but also suppresses precipitation in dust source regions over the eastern and southern Arabian  
40 Peninsula and northeastern Africa.

41 On the daily scale, in addition to the favorable large-scale condition associated with a  
42 negative PDO, enhanced atmospheric instability in Syria associated with increased precipitation  
43 in Turkey and northern Syria is also critical for the development of strong springtime dust storms  
44 in Syria.

45

46

47



## 48 1. Introduction

49 Dust aerosol is an important component in the climate system that can modify global and  
50 regional energy and water balances (e.g., Tegen et al., 1996; Miller and Tegen, 1998; Miller et  
51 al., 2004; Lau et al., 2009; Yue et al., 2010; 2011; Choobari et al., 2014; Huang et al., 2014).  
52 Dust particles interact with both solar and terrestrial radiation, modifying temperature profile and  
53 hydrological cycle, which impact regional and global climate. For instance, studies found that  
54 mineral dust influences the strength of the West African monsoon (e.g., Miller and Tegen, 1998;  
55 Miller et al., 2004; Yoshioka et al., 2007; Solmon et al., 2008; 2012; Mohowald et al., 2010;  
56 Strong et al., 2015) and Indian summer monsoonal rainfall (Vinoj et al., 2014; Jin et al., 2014,  
57 2015, 2016; Solmon et al., 2015; Kim et al., 2016). Dust particles can also serve as ice cloud  
58 nuclei and influence the microphysical and macrophysical properties of the cloud (e.g., Levin et  
59 al., 1996; Rosenfeld et al., 1997; Wurzler et al., 2000; Nakajima et al., 2001; Bangert et al.,  
60 2012), including its droplet size, number concentration, lifetime, albedo, and in turn affecting the  
61 regional radiative budget and hydrological cycle. Mineral dust also provides nutrients for ocean  
62 phytoplankton, affecting ocean productivity and therefore carbon and nitrogen cycles and ocean  
63 albedo (e.g., Fung et al., 2000; Shao et al., 2011). Strong dust storms also have severe social and  
64 health impacts (e.g., Morman and Plumlee, 2013), affecting public transportation and causing  
65 damage to the eye and lung.

66 The Middle East is one of the dustiest regions in the world, and recent study suggested an  
67 increasing trend of aerosol optical depth largely due to dust emission (e.g., Pozzer et al., 2015;  
68 Klingmüller et al., 2016). A once-in-ten-years severe dust storm recently occurred in Syria  
69 during September 6-9<sup>th</sup>, 2015, and raised many attentions. More than one thousand people in



70 Syria were hospitalized due to breathing difficulties<sup>\*</sup>. The causes of such a strong dust storm are  
71 not fully understood, but there have been speculations that the ongoing civil war in Syria is  
72 responsible for it. The argument is that crop fields were abandoned or destroyed by the war, so  
73 soil dust is easier to be uplifted by wind from these unprotected land fields. More importantly,  
74 will severe dust storms like the one above increase in the future?

75 Notaro et al. (2015) studied the dust activities over the Arabian Peninsula and related the  
76 increased dust activities during 2007-2013 to the persistent dry condition over the “Fertile  
77 Crescent” (namely Syria, Iraq, Israel, and Jordan) primarily caused by a combined effect of La  
78 Niña and a negative phase of Pacific decadal oscillation (PDO). Associated with the drought is  
79 crop failure and increased dust activities over the Arabian Peninsula. While others, such as Chin  
80 et al. (2014) found that the positive trend of dust emission over the Middle East from 2000-2009  
81 is related to increased surface wind speed, and Klingmüller et al. (2016) attributed the positive  
82 trend of aerosol optical depth (AOD) over the region (mainly Saudi Arabia, Iraq, and Iran) from  
83 2001-2012 to a combined effects of decreased precipitation and soil moisture over Iraq and  
84 adjacent areas and enhanced surface wind over the Africa Red Sea coastal area that increased  
85 dust emission.

86 The above studies suggested that remote sea surface temperature (SST), local  
87 precipitation, surface wind, and vegetation all influence the dust activities over the Middle East.  
88 Among these factors, the remote forcings, such as tropical Pacific SST, the PDO, not only affect  
89 the precipitation variations over the region but can also influence local circulation including near  
90 surface winds, both of which influence dust emission. It is thus quite important to understand the

---

\* <https://www.washingtonpost.com/news/worldviews/wp/2015/10/07/syrias-war-helped-create-an-epic-dust-storm-scientists-say/>



91 influences of these low-frequency long-lasting forcings on dust activities underlying the ongoing  
92 human perturbations such as civil war, land use change, and anthropogenic emission.

93 In this paper we examine the influence of the PDO on the variations of dust activities in  
94 Syria from 2003-2015 using Moderate Resolution Imaging Spectroradiometer (MODIS) Deep  
95 Blue dust optical depth (DOD). Previous studies on the connection between the PDO and dust  
96 activities in the Arabian Peninsula mainly focus on precipitation (e.g., Notaro et al., 2015; Yu et  
97 al., 2015). Here we explore thoroughly how the PDO influences the key factors associated with  
98 the dust activities in Syria on the interannual and daily scales.

99 The following section presents the data and methodology used in the paper. The co-  
100 variations of DOD in Syria and PDO are presented in sections 3 and their physical connections  
101 are analyzed in details in section 4. In section 5, we examined the key factors associated with  
102 strong spring dust events in Syria using daily reanalysis and observations. To what extend can  
103 climate models capture the connections between the PDO and Syrian dust activities is examined  
104 using the Geophysical Fluid Dynamics Laboratory (GFDL) AM3 model and discussed in section  
105 6. Major conclusions are summarized in section 7.

106

## 107 **2. Data and methodology**

### 108 **2.1 Satellite and observational datasets**

#### 109 **2.1.1 Dust optical depth**

110 Daily and monthly dust optical depth data is derived from MODIS aerosol products  
111 retrieved using Deep Blue (M-DB2) algorithm, which employs radiance from the blue channels  
112 to detect aerosols over bright land surface (e.g., desert). Because surface reflectance is low at  
113 blue channels, increases of reflectance and spectral contrast indicate the presence of aerosols



114 (Hsu et al., 2004, 2006). Ginoux et al. (2012) used collection 5.1 level 2 aerosol products from  
115 MODIS aboard Aqua satellite to derive DOD. Here, both MODIS aerosol products (collection 6,  
116 level 2) from the Aqua and Terra platforms are used for cross-validation. Terra passes the  
117 equator from north to south around 10:30 a.m. local time while Aqua passes the equator from  
118 south to north around 13:30 p.m. local time. While the frequency of the maximum daily 10 m  
119 wind in Syria peaks in the afternoon, later than the passing time of both Terra and Aqua, the  
120 averaged maximum total wind speed is nearly evenly distributed over a day (supplementary  
121 Figure S1). Thus, the results from both platforms are likely to provide a more complete picture of  
122 dust activities than either one alone.

123 Aerosol products such as AOD, single scattering albedo, Angström exponent are first  
124 interpolated to a regular  $0.1^\circ$  by  $0.1^\circ$  grid using the algorithm described by Ginoux et al. (2010).  
125 The dust optical depth is then derived from AOD following the methods of Ginoux et al. (2012)  
126 with adaptations for the newly released MODIS Collection 6 aerosol products. To separate dust  
127 from other aerosols, we use the Angström exponent, which has been shown to be highly sensitive  
128 to particle size (Eck et al., 1999) and single scattering albedo which is less than one for dust due  
129 to its absorption of solar radiation. Instead of using negative values of Angström exponent as by  
130 Ginoux et al. (2012), we use a continuous function relating Angström exponent to fine-mode  
131 aerosol optical depth established by Anderson et al. (2005; their Eq. 5) based on ground-based  
132 data. The DOD data is available from January 2003 to December 2015.

133 Daily and monthly DOD indices are formed by averaging DOD data in Syria between  
134  $34^\circ$ - $36.5^\circ$ N and  $36.5^\circ$ - $41^\circ$ E to characterize dust activities. The averaging area covers most region  
135 of Syria. We also tested using a smaller averaging box ( $33.5^\circ$ - $36^\circ$ N,  $36.5^\circ$ - $39^\circ$ E) for the DOD  
136 index, and the results are similar.



### 137 **2.1.2 Precipitation**

138 Version 7 of Tropical Rainfall Measurement Mission (TRMM) Multi-satellite  
139 Precipitation Analysis (TMPA) daily product (3B42) is used. This product covers from 50°S to  
140 50°N with a spatial resolution of 0.25° by 0.25° and is available from 1998 to present. Several  
141 important changes are applied to version 7 product, including using additional satellite data such  
142 as early record of Microwave Humidity Sounder (MHS) and operational Special Sensor  
143 Microwave Imager (SSM/I) record, using a new infrared brightness temperature dataset before  
144 the start of the Climate Prediction Center (CPC) 4-km Merged Global IR data set, using a single  
145 uniformly processed surface precipitation gauge analysis, using a latitude-band calibration  
146 scheme for all satellites, and adding output fields in the data files (Huffman and Bolvin, 2014).

147 Precipitation Reconstruction over Land (Chen et al., 2002; hereafter PRECL) from  
148 National Oceanic and Atmospheric Administration (NOAA) is a global analysis available monthly  
149 from 1948 to present at a 1° by 1° resolution. The dataset is derived from gauge observations  
150 from the Global Historical Climatology Network (GHCN), version 2, and the Climate Anomaly  
151 Monitoring System (CAMS) datasets.

152 The monthly precipitation of the Climatic Research Unit (CRU) time-series (TS) 3.23  
153 (Harris et al. 2014) is also used as a supplement to the PRECL. CRU TS 3.23 dataset covers  
154 1901-2014, with a spatial resolution of 0.5° by 0.5° over land (excluding Antarctica). The  
155 gridded data is based on the analysis of over 4,000 individual weather station records.

156

### 157 **2.1.3 Temperature**

158 The Hadley Centre sea ice and sea surface temperature (HadISST) data set (Rayner et al.,  
159 2003) from the UK Met Office is available monthly from 1870 to the present with a horizontal



160 resolution of  $1^\circ$  by  $1^\circ$  grid. Monthly SST from HadISST and land surface temperature from CRU  
161 TS 3.23 ( $0.5^\circ$  by  $0.5^\circ$ ) from 1948-2015 are used to examine temperature patterns associated with  
162 dust activities.

163

#### 164 **2.1.4 Leaf area index (LAI)**

165 LAI characterizes the canopies of plants. It is defined as the one-sided green leaf area per  
166 unit ground area in broadleaf canopies and as half the total needle surface area per unit ground  
167 area in coniferous canopies. LAI at zero is considered as bare ground while around 10, dense  
168 forests. Monthly LAI is derived from the version 4 of Climate Data Record (CDR) of Advanced  
169 Very High Resolution Radiometer (AVHRR) surface reflectance (Claverie et al., 2014) and  
170 produced by the National Aeronautics and Space Administration (NASA) Goddard Space Flight  
171 Center (GSFC) and the University of Maryland. The gridded monthly data is on a  $0.05^\circ$  by  $0.05^\circ$   
172 horizontal resolution and available from 1981 to present. A detailed discussion on the algorithm  
173 and evaluation of the dataset can be found by Calverie et al. (2016).

174 Monthly MODIS LAI level 4 data on the Aqua platform (MYD15A2) is also used for  
175 2003-2015. The original data files were obtained via personal communication (Ranga Myneni  
176 and Taejin Park; Boston University) and then reprocessed to fill the missing data by Paul  
177 Ginoux. The horizontal resolution of the data is  $0.1^\circ$  by  $0.1^\circ$  degrees.

178

#### 179 **2.2 Reanalyses**

180 Daily and monthly geopotential height, horizontal winds, specific humidity from the  
181 National Centers for Environmental Prediction (NCEP)/National Center for Atmospheric  
182 Research (NCAR) reanalysis (Kalnay et al., 1996, hereafter NCEP1) from 1948 to 2015 are used.



183 Its horizontal resolution is  $2.5^\circ$  by  $2.5^\circ$  and have 17 vertical levels from 1000 hPa to 10 hPa, with  
184 8 levels between 1000 hPa and 300 hPa. This reanalysis is used primarily in this study due to its  
185 long record.

186 ERA-interim (Dee et al., 2011) from the European Centre for Medium-Range Weather  
187 Forecasts (ECMWF) is a global reanalysis with a horizontal resolution of T255 (about  $0.7^\circ$  or 80  
188 km) and 37 vertical levels, available from 1979 to present. Monthly and four (two) times daily  
189 analysis (forecast) variables are used. The time coverage of ERA-Interim is shorter than the  
190 NCEP1 but its high resolutions supplements the latter. Monthly horizontal winds and  
191 geopotential heights are compared with the NCEP1 in the same period (1979-2015) and show  
192 similar features (see discussion in section 3). Daily 10 meter and 850 hPa winds, and forecast  
193 variables such as precipitation are used to investigate the key factors associated with dust  
194 activities.

195

### 196 **2.3 Climate indices**

197 The PDO and Niño3.4 indices are downloaded from the website of NOAA Climate  
198 Prediction Center (<http://www.esrl.noaa.gov/psd/data/climateindices/list/>). The monthly  
199 standardized PDO index is derived from the leading principal component of SST anomalies in  
200 the northern Pacific Ocean ( $20^\circ\text{N}$  north). The monthly mean of global mean SST anomalies are  
201 removed in the PDO index, thus the influence of global warming is not included. The data is  
202 available from 1948 to present. The monthly Niño 3.4 index is derived from the extended  
203 reconstructed sea surface temperature (ERSST v4; Huang et al., 2015; Lui et al., 2015; Huang et  
204 al., 2016) averaged over the tropical Pacific between  $5^\circ\text{N}$ – $5^\circ\text{S}$  and  $120^\circ$ – $170^\circ\text{W}$  and is available  
205 from 1950 to present.



## 206 **2.4 Model output**

207 To examine the relationship between the Syrian dust activities and the PDO, the output  
208 from the atmospheric component (AM3) of a general circulation model (CM3; Donner et al.,  
209 2011) developed at the GFDL is used. The finite-volume algorithms described in Lin and Rood  
210 (1996, 1997) and Lin (1997, 2004) is used in the dynamic core in AM3. Different from earlier  
211 versions of the model, a general curvilinear coordinate system is used and largely improved the  
212 computational efficiency. A hybrid vertical coordinate (Simmons and Burridge, 1981) of 48  
213 layers is used, with the top model layer at about 1 Pa (~86 km). AM3 calculates the mass  
214 distribution and optical properties of aerosols according to their emission, chemical production,  
215 transport, and dry and wet deposition. The dust source function follows the scheme of Ginoux et  
216 al. (2001), which places preferential sources in topographic depressions. The simulated aerosol  
217 optical depth and co-albedo show improved correlations with the AErosol RObotic NETwork  
218 (AERONET) station observations than earlier version of the model (CM2.1) but slightly  
219 underestimate AOD in the Middle East.

220 A historical run is conducted using the observed monthly SSTs from the Hadley center to  
221 drive the AM3. The simulated wind is nudged toward the NCEP/NCAR reanalysis with a  
222 relaxation timescale of 6 hours (Moorthi and Suarez, 1992), similar to the method used by Li et  
223 al. (2008). A moderate horizontal resolution of  $2^\circ$  by  $2.5^\circ$  is used. The simulation was conducted  
224 from 1948 to 2010. Results from 1960 to 2010 are presented.

225

## 226 **3. The co-variations between springtime DOD in Syria and the PDO during 2003-2015**

227 Notaro et al. (2015) related low-frequency variations of monthly precipitation over Syria  
228 and Iraq to the El Niño–Southern Oscillation (ENSO) and the PDO and thus built the connection



229 between dust activities and Pacific SSTs. Here we focus on Syria. Figure 1 shows the time series  
230 of monthly Syrian DOD indices (seasonal cycle removed) from both MODIS Aqua (green) and  
231 Terra (grey) platforms and the negative PDO index from January 2003 to December 2015. The  
232 variations of the DOD and the negative PDO indices are quite similar, showing strong decadal  
233 variations underlying interannual variations. Both are relatively weak during 2003-2007,  
234 relatively strong during 2007-2012 and become relatively weak since 2013. Note that the DOD  
235 indices increase again in 2015 in association with the severe dust storm in September. The  
236 correlation between monthly DOD indices and PDO index are -0.51 (Aqua) and -0.50 (Terra)  
237 from 2003-2015. Other indices, such as Niño 3.4 and Syrian LAI also have significant but lower  
238 correlations with the DOD indices (Table 1).

239 ENSO is known to influence precipitation over the Middle East, by decreasing  
240 precipitation in La Niña years and increasing precipitation in El Niño years (e.g., Price et al.,  
241 1998; Mariotti et al., 2005; 2007, Chakaborty et al., 2005; Barlow et al., 2002, Wang et al., 2014;  
242 Yu et al., 2015; Banerjee and Kumar, 2016), and its influence is generally stronger in La Niña  
243 years (e.g., Wang et al., 2014). Previous study also showed a comparable influence of the PDO  
244 on precipitation over the “Fertile Crescent” region including Syria and Iraq versus that by ENSO  
245 (correlations of 0.52 versus -0.57 from 1979-2013, Notaro et al., 2015). The correlations in this  
246 study indicate that the PDO plays a greater role than ENSO in modulating dust activities in Syria  
247 in the recent decade. The PDO is not completely independent of ENSO, but can be viewed as a  
248 phenomenon driven by multiple physical processes, including the tropical Pacific SST,  
249 atmospheric noise, Aleutian low, Kuroshio-Oyashio Extension, Pacific-North American pattern,  
250 Rossby wave breaking and etc. (e.g., Evans et al., 2001; Newman et al., 2003; Schneider and  
251 Cornuelle, 2005; Strong and Magnusdottir, 2009; Mills and Walsh, 2013). While some modeling



252 studies suggested that up to half of the variance of the PDO can be explained by ENSO (e.g.,  
253 Alexander et al., 2002; Liu and Alexander, 2007), others found that there certain part of extra-  
254 tropical Pacific SST variability are totally independent of ENSO (e.g., Zhang et al., 1997; Deser  
255 and Blackmon, 1995; Zhang and Delworth, 2015). Here the correlation between the monthly  
256 PDO and Niño 3.4 indices is 0.63 from January 2003 to December 2015, suggesting that  
257 statistically the Niño 3.4 index explains about 40% of the variances of the PDO index.

258 Figure 2 shows the correlation between the PDO index and Aqua and Terra DODs in  
259 spring, along with correlations between the Syrian DOD indices and PDO index in individual  
260 month and on annual mean from 2003-2015. The correlation pattern between the PDO index and  
261 Aqua DOD is very similar to that associated with Terra DOD (Figs. 2a-b), with negative  
262 correlations over most areas of Syria and a stronger correlation over the eastern Syria than the  
263 western part. DOD over Iraq and northern Saudi Arabia is also significantly negatively correlated  
264 with the PDO. The correlation between the monthly PDO and Syrian DOD indices shows a  
265 persistent negative relationship through the year, with higher correlations during March-April-  
266 May and also in July-August and December (Fig. 2c). The low correlation in September is due to  
267 the severe dust storm in 2015. The seasonal mean correlations between the DOD indices and the  
268 PDO index in MAM are -0.90 for both the Aqua DOD and Terra DOD indices, again much  
269 higher than their correlations with other indices (Table 2).

270 The connection between the Syrian DOD and PDO is further examined in Figure 3,  
271 which shows the correlations between the Syrian DOD indices and SST and land surface  
272 temperatures during MAM and on the annual mean, along with SST and land surface  
273 temperature patterns associated with the PDO index. As shown in Figs. 3a-b, the SST pattern  
274 associated with the positive phase of the PDO in spring are quite similar to that in the annual



275 mean, with anomalous warm SST over the tropical Pacific and along the east basin of North  
276 Pacific and anomalous cold SST over the subtropical central to western North Pacific. SST in the  
277 India Ocean is also positively associated with the PDO. But the correlation between land surface  
278 temperature and the PDO is not significant in most regions, including the Arabian Peninsula.

279 Correlations between Aqua DOD index and SST in MAM are nearly opposite to those of  
280 the PDO, with negative correlations over the tropical and eastern Pacific but positive correlations  
281 over the central North Pacific (Fig. 3c). Correlations between the annual mean Aqua DOD index  
282 and SST and land surface temperature are similar to that in spring, but with slightly weaker  
283 magnitude over the central Pacific (Fig. 3d). The temperature patterns correlated with the Terra  
284 DOD index are quite similar to that of Aqua DOD index (Figs. 3e-f). Both DOD indices are not  
285 significantly correlated with the land surface temperature over the Middle East in spring.

286 Since Figs. 2-3 indicate a stronger negative correlation between the PDO and Syrian  
287 DOD index during MAM than on annual mean or other seasons, the following analysis focuses  
288 on their connections in spring. Spring is also the time when Syrian DOD is high and dust storms  
289 are most active (supplementary Figures S2-3).

290

#### 291 **4. How does the PDO affect Syrian dust activities in spring?**

292 In this section we explore the mechanisms underlying the strong negative correlations  
293 between the PDO and Syrian DOD indices. Since MODIS DOD only covers the recent decade  
294 and the PDO has low-frequency decadal variations with cycles of about 15-25 and 50-70 years  
295 (e.g., Minobe, 1997; Mantua and Hare, 2002), it is difficult to assess their long-term (i.e., beyond  
296 the recent decade) relationship directly. To establish their connections, we first compare the  
297 patterns of circulation and precipitation associated with DOD and PDO indices during 2003-



298 2015. The patterns associated with long-term variations of the PDO (e.g., 1948-2015 from the  
299 NCEP1 or 1979-2015 from the ERA-interim) are then examined and compared with those  
300 associated with the PDO in the recent decade. The PDO shows a dominant negative phase during  
301 the late 1940s to 1970s and turns into a dominant positive phase during the 1980s and 1990s and  
302 becomes mostly negative again since the middle 2000s (e.g., JISAO/University of Washington  
303 website<sup>†</sup>). Therefore the NCEP1 reanalysis covers about one 50-70 years multi-decadal cycle of  
304 the PDO, while the EAR-Interim covers about half of the cycle. Assuming that the factors  
305 dominated the variations of Syrian DOD persist beyond the recent decade (e.g., also valid during  
306 1948-2015), then the similarity between the patterns associated with the PDO in the recent  
307 decade and those over longer time periods would indicate a persistent influence of the PDO on  
308 dust activities in Syria.

309 How does the PDO affect the circulation over the Middle East? Figure 4 shows the  
310 regression of 200 hPa (contours) and 850 hPa (shading) geopotential heights onto the  
311 standardized PDO and DOD indices. Fig. 4a shows in the positive phase of PDO, stationary  
312 wave propagates from the North Pacific through North America, northern Atlantic and Europe to  
313 the Middle East. The regressions at 850 hPa are generally similar to those at 200 hPa, indicating  
314 an equivalent barotropic structure. Anomalous positive geopotential height over the Arabian  
315 Peninsula is associated with a positive PDO during 2003-2015 (Fig. 4a) and also during 1948-  
316 2015 (Fig. 4c). The geopotential height patterns associated with the both Aqua and Terra DOD  
317 indices are nearly opposite to those associated with the positive PDO index, with anomalous high  
318 over the central North Pacific and northeastern North America and anomalous low over the west  
319 coast of North America and Europe and the Middle East (Figs. 4b, d).

---

<sup>†</sup> <http://research.jisao.washington.edu/pdo/graphics.html>



320 Fig. 4 suggests that the PDO can influence the variations of springtime DOD in Syria  
321 through its modification on the circulation over the Middle East. A negative PDO reduces the  
322 geopotential height both at 850 and 200 hPa over the Arabian Peninsula, a scenario that favors  
323 high DOD in spring.

324 The connection between Syrian DOD and 850 hPa winds and geopotential heights are  
325 further examined in Figure 5. Fig. 5a shows that a positive PDO is associated with anomalous  
326 easterly winds north of 40°N, anomalous northerly winds over the central Mediterranean Sea  
327 around 15°E and weak southeasterly winds over the eastern Mediterranean Sea and western  
328 Syria in the recent decade (Fig. 5a) and from 1948-2015 (Fig. 5c). Anticyclonic winds are  
329 located over Oman and Yemen at the south coast of Arabian Peninsula accompanied by an  
330 anomalous high. Positive geopotential height anomalies are also located over the northwestern  
331 Africa, and East Africa. On the other hand, winds associated with high Syrian DOD indices are  
332 anomalous westerly over the northern Mediterranean basin and Syria (Figs. 5b and d).  
333 Anomalous cyclonic flows are located over the southern Arabian Peninsula, nearly opposite to  
334 that associated with the positive phase of the PDO. The overall lower geopotential height over  
335 the Middle East and Africa also facilitate the formation of the cyclones (such as Sharav  
336 cyclones) that are important for the spring peak of dust storms in the northern Arabian Peninsula  
337 (e.g., Shao et al. 2001; Israelevich, et al. 2003; Dayan et al. 2008; Dayan et al. 2012).

338 The regression patterns of 850 hPa winds and geopotential height onto the PDO and  
339 DOD indices in the ERA-Interim are generally consistent with those shown in the NCEP1  
340 (Supplementary Figure S4).

341 Next we examine the associated variations of near surface wind and precipitation that are  
342 tied to these geopotential height and low-level wind patterns. Figure 6 shows the regression of



343 10 m winds (vectors) and the cubic 10 m wind speed (shading) in the ERA-Interim onto  
344 standardized PDO index and onto the Aqua and Terra DOD indices. The ERA-Interim is chosen  
345 here because of its higher horizontal resolution compared to the NCEP1, and thus is more  
346 suitable to examine surface wind variations associated with dust blasting in small scales. Cubic  
347 wind speed is used here as classical dust emission scheme relates dust flux to the third power of  
348 10 m horizontal winds. The patterns of the surface wind associated with the DOD indices (Figs.  
349 6b and d) are largely similar to that of winds at 850 hPa (Figs. 5 and S4). Anomalous  
350 southwesterly winds from coastal North Africa and over the Mediterranean Sea tend to bring  
351 dust from North Africa to Syria. Such a route of dust transport has not been directly examined,  
352 but was discussed in back trajectories studies on the airflow patterns onto Israel (e.g., Dayan,  
353 1986). Earlier studies also have suggested a transport of dust from North Africa to the  
354 Mediterranean basin (e.g., D'Almeida, 1986; Moulin et al., 1998; Kubilay et al., 2000).  
355 Anomalous northerly flow over the Red Sea and the west coast of the Arabian Peninsula (and a  
356 weaker wind speed) and anomalous southerly flow (and a stronger wind speed) over the eastern  
357 Peninsula also suggest a transport of dust from the source regions in the middle and southern  
358 Arabian Peninsula, e.g., An Nafud and Ad Dahna deserts, dry riverbeds such as Al Batin, Al-  
359 Rimah, and Al Sahba and Rub's al Khali Sandy desert in Saudi Arabia (Ginoux et al., 2012). An  
360 Nafud and Ad Dahna deserts are major sources of dust storms in Saudi Arabian in spring to early  
361 summer (Notaro et al., 2013) and can also be an important source for Syrian DOD. A modeling  
362 study on the sources of spring DOD in Syria also confirms that North Africa (including Libya,  
363 Algeria, and Egypt) is the largest source with the secondary source from the Arabian Peninsula  
364 (Iraq and Saudi Arabia), and the overall transported DOD is much higher than local DOD in  
365 Syria in spring (Ginoux et al., in preparation).



366 Variations of surface wind associated with the PDO are different from that associated  
367 with high DOD, with nearly opposite pattern of cubic wind speeds over the Arabian Peninsula  
368 (Figs. 6a and c). When the PDO is positive, anomalous northerly winds pass through the  
369 Mediterranean Sea and turn into westerly over the northeastern Africa, which may bring dust  
370 from Africa to Israel, Jordan, and Syria as well as increase the moisture transport from the  
371 Mediterranean Sea (Fig. 6a). The anomalous southerly wind from the Red Sea also brings  
372 moisture onto Syria and tends to promote precipitation. Over southwestern Syria, the anomalous  
373 southerly wind is from the less dusty area over northwestern Saudi Arabia and is less likely to  
374 enhance Syrian DOD. A weak anomalously westerly flow over the northeastern Saudi Arabia  
375 around 30°N and 45°E tends to block the northward transport of dust from the southern and  
376 middle Arabian Peninsula to Syria. This westerly flow weakens if extending the time period of  
377 regression to 1979 (Fig. 6c). A stronger anomalously westerly flow along the west coast of Saudi  
378 Arabia and a southerly flow from the south coast of the Arabian Peninsula are also found in  
379 association with the positive PDO during 1979-2015, bringing moisture onto Syria. The  
380 discrepancies between the regression patterns in the recent decade and those during 1979-2015,  
381 e.g., over the eastern Mediterranean Sea (Figs. 6a and c), are likely associated with the decadal  
382 variations of the PDO, indicating an instable connection between the PDO and surface winds in  
383 some areas.

384 The anomalous precipitation pattern correlated with the PDO and DOD indices are shown  
385 in Figure 7. The PDO has a mild connection with precipitation over the Middle East in spring on  
386 the interannual time scale. Similar correlation patterns are found in previous studies that  
387 correlated the PDO with low-frequency (i.e., >7years) variations of precipitation (e.g., Dai, 2013,  
388 Fig. 2c). A positive phase of the PDO is associated with increased precipitation over most area of



389 the Arabian Peninsula, Turkey, western Iran, and northeastern Africa over Libya and Egypt in  
390 the recent decade and during 1948-2015 (Figs. 7a and c). Patterns are similar during 1979-2015  
391 (not shown). On the other hand, high DOD in Syria is associated with reduced precipitation over  
392 the Arabian Peninsula (particularly, Iraq, central and southern Saudi Arabia), Egypt, eastern  
393 Algeria, and western Libya. This is consistent with Fig. 6, which indicates dust transport from  
394 these areas to Syria in the spring.

395 Figure 8 shows the vertically integrated mass-weighted moisture flux (vector) and its  
396 magnitude (shading) onto the standardized PDO and DOD indices in MAM from 2003-2015 and  
397 also onto the PDO index during 1948-2015. Consistent with the precipitation regression patterns  
398 (Fig. 7), anomalous anticyclonic moisture flux brings more moisture onto the Arabian Peninsula  
399 from the Red Sea and Gulf of Aden associated with a positive PDO (Figs. 8a and c). Moisture  
400 flux over the northeastern Africa is also enhanced. Oppositely, high DOD in Syria is associated  
401 with an anomalous cyclonic flux centered over the south coast of the Arabian Peninsula, which  
402 reduces moisture flux onto the southern Arabian Peninsula (Figs. 8b and d). Moisture flux over  
403 northeastern Africa is also reduced associated with an anomalous cyclonic flow over Sudan and  
404 Egypt. The pattern of the anomalous moisture fluxes associated with PDO and DOD indices are  
405 quite similar to that of the 850 hPa winds (e.g., Fig 5), indicating a dominant role played by low-  
406 level moisture transport.

407 These anomalous circulation and moisture flux patterns are also linked to the stability of  
408 lower atmosphere. Figure 9 shows the regression of low-level Moist Static Energy (MSE;  
409 integrated from surface to 700 hPa) onto the standardized PDO and DOD indices. MSE is  
410 defined as a sum of sensible, latent, and geopotential energy in a column air, i.e.,  $MSE =$   
411  $c_p T + Lq + gz$ , where  $c_p$  is the specific heat of air at constant pressure,  $T$  is air temperature,  $L$  is the



412 latent heat of vaporization of water,  $q$  is specific humidity, and  $g$  is the gravity acceleration, and  $z$   
413 geopotential height. MSE increasing with altitude denotes a stable atmosphere, so high MSE in  
414 the lower atmosphere indicates an instable condition, and vice versa. The patterns of the  
415 anomalous MSE are tied to the changes of moisture flux and precipitation anomalies. Reduced  
416 MSE is located over large areas of the Arabian Peninsula, particularly, the southwest coast, in  
417 association with high DOD in Syria, indicating a more stable low-level atmosphere and thus less  
418 precipitation (Fig. 9b and d). Such a low MSE is also found over North Africa, but in a weaker  
419 magnitude. The pattern associated with a positive PDO is nearly opposite, with increased low-  
420 level MSE over the Arabian Peninsula, Red Sea, and along the east coast Egypt, denoting an  
421 instable atmosphere associated with anomalous moisture transport (Figs. 8a and c) and  
422 promoting convection and precipitation (Figs. 9a and c).

423 In short, Figs. 4-9 show spring circulation and precipitation patterns favorable to high  
424 DOD in Syria. Anomalous low pressure over Europe, the southern Arabian Peninsula, and  
425 northeastern to eastern Africa promotes westerly winds from North Africa and southerly flow  
426 over the southeastern Arabian Peninsula, both of which tend to transport dust to Syria. The  
427 anomalous moisture fluxes associated with the geopotential height and wind anomalies also  
428 favor a dry and stable condition over the dust source regions adjacent to Syria, such as Saudi  
429 Arabia, Iraq, and North Africa. The circulation and precipitation patterns associated with a  
430 positive PDO are largely opposite to those associated with high DOD in Syria in the recent  
431 decade, which explains the strong negative correlation between the two. Examination on  
432 circulation and precipitation variations associated with the PDO in a longer time period (either  
433 from 1979-2015 or 1948-2015) show generally similar patterns, but also with some  
434 discrepancies. If the conditions associated with high DOD in Syria are valid beyond the recent



435 decade, i.e., 2003-2015, the negative role of the PDO on spring dust activities in Syria is also  
436 likely to persist.

437

#### 438 **5. Analysis on strong dust storms in spring**

439 Severe dust storms usually only persist a few days or even a few hours (e.g., Haboobs)  
440 and seasonal or monthly averages reduce the variability of dust activities and may smooth out  
441 some important features. In this section we discuss the conditions associated with strong dust  
442 storms in Syria using daily DOD and reanalysis variables and compare these conditions with  
443 those from seasonal mean patterns discussed above including the teleconnections with the PDO.  
444 Composites are formed based on daily Syrian DOD index from Aqua. Days during March, April,  
445 and May from 2003-2015 are selected when the DOD index is greater than 1 standard deviation  
446 to form daily composites. Results are very similar but patterns are in slightly stronger (weaker)  
447 magnitudes if choosing the threshold of 1.5 (0.5) standard deviations (not shown).

448 Figure 10 shows the composite of Aqua and Terra daily DOD (shading) and ERA-Interim  
449 10 m winds based on the Aqua DOD index. The patterns are quite similar in Aqua and Terra  
450 DODs. DOD anomaly is above 0.3 over Syria and western Iraq (Figs. 10a-b). Anomalous high  
451 DOD is also located over eastern Saudi Arabia and the northeastern Africa, indicating a possible  
452 transport of dust from these areas to Syria. Anomalous cyclonic flow is centered over southern  
453 Turkey around 30°E, with anomalous strong westerly wind blowing from North Africa and  
454 southerly flow from the eastern Arabian Peninsula, consistent with dust transport discussed in the  
455 above section. However, different from the seasonal mean regression patterns (e.g., Fig. 6), there  
456 are the anomalous southerly winds from the Red Sea and Persian Gulf.



457 Figure 11 shows the composite of daily precipitation from ERA-Interim two times daily  
458 forecast and TRMM daily precipitation for days with DOD anomaly above 1 standard deviation.  
459 Precipitation anomalies are shown in percentages (with reference to the climatological mean)  
460 instead of absolute values in order to highlight the precipitation variations over the Middle East,  
461 where the magnitude of precipitation in spring is quite low (less than  $1 \text{ mm day}^{-1}$  in most of the  
462 areas). Patterns of precipitation anomalies associated with strong dust storms are quite similar in  
463 the ERA-Interim and TRMM, but with greater magnitudes in the ERA-Interim. Precipitation  
464 increases significantly (about 80% in TRMM and more than 100% in the ERA-Interim) over  
465 Turkey and the northeastern Mediterranean, but decreases over the central and southern Arabian  
466 Peninsula and northeastern Africa. Syria sits in between the anomalous wet and dry regions, with  
467 slightly increased precipitation in its northern domain. These features are somewhat similar to  
468 the results of previous studies on strong dust storms and our understanding on the seasonal mean  
469 patterns associated with high DOD in Syria. Strong dust storms such as Haboobs (usually about  
470 1 kilometer height and tens to hundreds of kilometer length) are usually associated with  
471 convective storms (e.g., Miller et al., 2008; Roberts and Knippertz, 2012; Vukovic et al., 2014;  
472 Dempsey, 2014). The cold downdraughts from convective storms spread out and can lift the dust  
473 from the surface to form a dusty towering “wall” as the front of a Haboob. Similarly, severe  
474 precipitation and convection in Turkey and northern Syria can produce an unstable atmospheric  
475 condition in the region, and the intensified low-level winds can lift dust from the surface and  
476 thus increase DOD. Reduced precipitation over southern Arabian Peninsula and North Africa  
477 facilitates dust transport from these source areas to Syria.

478 Figure 12 shows composites for vertically integrated mass weighted moisture flux  
479 (vectors) and its magnitude (shading) from the NCEP1 and convective available potential energy



480 (CAPE) from the ERA-Interim for days with Aqua DOD index greater than 1 standard deviation.  
481 Fig. 12a shows anomalous westerly flux from northern Egypt and southerly flux from the Red  
482 Sea and Persian Gulf largely increase the moisture transport to Syria and eastern Turkey, while  
483 the reduced moisture fluxes along the south coast of Iran, southern Arabian Peninsula, southern  
484 Red Sea, and the Gulf of Aden are quite similar to those patterns association with high Syrian  
485 DOD in spring (Figs. 8b and d) and a negative PDO (i.e., opposite to Fig. 8c). Consistently,  
486 CAPE is increased over Turkey and Syria, indicating an unstable atmospheric condition  
487 associated with increased moisture transport to the region, while over southern Arabian  
488 Peninsula and northeastern Africa where moisture flux is reduced CAPE is decreased (Fig. 12b).

489 The connection between the PDO and daily strong dust storms is also verified by  
490 correlating an index of the occurrence of strong dusty events (i.e., daily DOD anomaly greater  
491 than 1 standard deviation) in MAM with HadISST from 2003-2015 (supplementary Figure S5).

492 Figs. 10-12 suggest that severe dust storms occur under both favorable large-scale and  
493 regional-scale features. Remote forcing such as PDO modifies springtime circulation and  
494 precipitation patterns, e.g., a negative phase of PDO decreases precipitation over the southern  
495 Arabian Peninsula, northeastern Africa and favors the transport of dry dusty air from these  
496 regions to Syria, while strong convective storms over Turkey favor the dust lifting and formation  
497 of strong dust storms in Syria.

498

## 499 **6. Can the recent GFDL climate model capture the connection between the PDO and** 500 **Syrian DOD?**

501 To what extent can current climate model capture the connection between the PDO and  
502 DOD? We examined such relationships in the GFDL AM3 model. Figure 13a shows the



503 correlation between modeled DOD index and surface temperature from 1960-2010 in MAM. The  
504 correlation pattern over the North Pacific is quite similar to that of a negative PDO (e.g., Fig. 3c),  
505 but only significant over the northern North Pacific, indicating a weaker such connection in the  
506 model. Over land, DOD is highly positively associated with surface temperature in the northern  
507 to northeastern Africa, which is not seen in the observations, and may suggest an overestimation  
508 of the connection in the model. The correlation pattern is similar if calculated from 1951 to 2010,  
509 but with a slightly stronger positive correlation over the tropical eastern Pacific (not shown).

510 Fig. 13b shows the regression of standardized DOD index onto 200 hPa (contours) and  
511 850 hPa geopotential heights (shading) during MAM 1960-2010. The wave trains propagation  
512 from north Pacific to the Middle East is quite similar to that shown in the NCEP1 using observed  
513 DOD index (Figs. 4b and d) but in a weaker magnitude in the tropical and subtropical North  
514 Pacific, consistent with the weak SST correlations (Fig. 13a). The anomalous low over Africa  
515 dips down to the eastern Sahel, probably in association with the biased correlation between the  
516 DOD and surface temperature over the northeastern Africa.

517 Figure 13 suggests that AM3 can partially capture the connection between the dust  
518 activities in Syria and the PDO. A few reasons may contribute to this underestimation. First,  
519 AOD is slightly underestimated in the Middle East compared with AERONET, and the simulated  
520 DOD is also less than that in MODIS, which indicates that dust variability may be  
521 underestimated in the region. Current dust scheme in AM3 only relates dust emission to dust  
522 source map and surface wind speed, while the influence of soil moisture on dust emission is not  
523 explicitly considered. Thus, the anomalous dust transport from southern Arabian Peninsula and  
524 northeast Africa in association with the dry conditions under a negative PDO may not be  
525 captured by the model. Our analysis also suggest that the DOD in the model is highly correlated



526 with dry deposition over the western Mediterranean, along the north coast of Egypt, and Turkey  
527 and with the southwesterly winds in these region, indicating an very strong connection with the  
528 dust sources in Africa, which may be an overestimation. A new dust emission scheme that  
529 considers the influences of soil moisture and vegetation cover and land use change is currently  
530 under development, and the relationship between Syrian DOD and PDO is likely to be better  
531 represented in this newer version of the model.

532

## 533 7. Conclusions

534 Dust activities in the Middle East have been related to a lot factors, such as remote sea  
535 surface temperatures, near surface winds, and precipitation variability. The ongoing civil war and  
536 a recent severe dust storm in Syria in 2015 raised concerns as whether dust activities will  
537 increase in the region. First step toward answering this question is to understand the dust  
538 activities driven by the natural climate variability. Here we examine the connection between  
539 Syrian dust activities and the Pacific decadal oscillation (PDO) using innovative dust optical  
540 depth (DOD) datasets retrieved from MODIS Deep Blue aerosol products and multiple  
541 observations and reanalyses.

542 A significantly negative correlation is found between Syrian DOD and the PDO in  
543 springtime during 2003-2015, suggesting that the PDO index explains about 81% variances of  
544 Syrian DOD in spring in the recent decade. Such a connection is revealed not only on  
545 precipitation as emphasized by previous studies (e.g., Yu et al., 2014; Notaro et al., 2015) but  
546 also on other aspects such as the circulation patterns and surface winds. It is found that high  
547 DOD in Syria during spring is associated with low geopotential height over Europe, southern  
548 Arabian Peninsula, and northeastern to eastern Africa. Associated with these anomalous height



549 patterns are the westerly wind anomalies over the Mediterranean basin and southerly wind  
550 anomalies over the southeastern Arabian Peninsula, favoring dust transport from these regions to  
551 Syria, where the transported dust dominates the DOD in spring (Ginoux et al., in preparation). A  
552 positive PDO is connected with wind and height patterns largely opposite to those associated  
553 with high DOD over Syria. Positive phase of the PDO also tends to increase precipitation over  
554 the Arabian Peninsula and northeastern Africa via anomalous moisture transport that increases  
555 moisture supply and also reduces the stability of low-level atmosphere. A negative PDO thus is  
556 not only associated with wind and geopotential height patterns favorable to high DOD in Syria  
557 but also tends to reduce precipitation in the dust source regions such as Iraq, Saudi Arabia, and  
558 northeastern Africa, and thus favors dust transport to Syria. This explains why the correlation  
559 between the Syrian DOD index and the PDO index is much higher than other individual index  
560 such as precipitation, leaf area index, and 10 m winds in Syria (Tables 1-2). The influences of the  
561 PDO on circulation and precipitation patterns over the Middle East largely persist beyond the  
562 recent decade, i.e., over 1948-2015, but also show some exceptions. The lack of long-term  
563 observations also brings uncertainties to the connection between the PDO and Syrian DOD.

564 Different from the patterns on seasonal mean discussed above, analysis on the daily  
565 composites of strong spring dust storms shows both the influence of the PDO and local features.  
566 In spring, strong dust storms (DOD anomalies greater than 1 standard deviation) in Syria is  
567 associated with an anomalous cyclonic flow centered over the northeastern Mediterranean Sea  
568 and Turkey, and southerly wind anomalies from the Red Sea and Persian Gulf. Consistently,  
569 moisture flux onto Turkey and Syria is enhanced and thus destabilizes the atmosphere and  
570 promotes precipitation in Turkey and convection and dust uplifting in Syria. Meanwhile, reduced  
571 moisture fluxes onto the southern Arabian Peninsula and east coast of Egypt and Sudan in



572 association with a negative PDO favor a dry and stable condition in Saudi Arabia and  
573 northeastern Africa, facilitating dust transport from these regions to Syria.

574 We examined the teleconnection between the DOD and PDO in the GFDL AM3 model.  
575 A weaker connection compared to that in the observation is found, which may be partially  
576 related to model's underestimation of the mean DOD and its variability in this area. The new  
577 dust scheme that includes the influence of soil moisture and precipitation is likely to overcome  
578 these drawbacks and provide a better representation of the relationship between Syrian DOD and  
579 the PDO.

580

581

582

583

584

585

586

587

588

589

590

591

592

593

594

595 *Acknowledgements.*

596 PRECL Precipitation data is provided by the NOAA/OAR/ESRL PSD, Boulder,  
597 Colorado, USA, from their Web site at <http://www.esrl.noaa.gov/psd/>. PDO and Niño3.4 indices  
598 are downloaded from the website of NOAA Climate Prediction Center  
599 (<http://www.esrl.noaa.gov/psd/data/climateindices/list/>). The NCEP/NCAR reanalysis product  
600 was obtained from <http://www.esrl.noaa.gov/psd/data/gridded/data.ncep.reanalysis.html> and the  
601 ERA-Interim is downloaded from [http://www.ecmwf.int/en/research/climate-reanalysis/era-](http://www.ecmwf.int/en/research/climate-reanalysis/era-interim)  
602 [interim](http://www.ecmwf.int/en/research/climate-reanalysis/era-interim). HadISST is downloaded from  
603 <http://www.metoffice.gov.uk/hadobs/hadisst/data/download.html> while CRU TS 3.23  
604 temperature and precipitation are downloaded from  
605 [https://crudata.uea.ac.uk/cru/data/hrg/cru\\_ts\\_3.23/cruts.1506241137.v3.23/](https://crudata.uea.ac.uk/cru/data/hrg/cru_ts_3.23/cruts.1506241137.v3.23/). The MODIS Deep  
606 Blue aerosol products were acquired from the Level-1 and Atmosphere Archive and Distribution  
607 System (LAADS) Distributed Active Archive Center (DAAC), located in the Goddard Space  
608 Flight Center in Greenbelt, Maryland (<https://ladsweb.nascom.nasa.gov/>). This research was  
609 supported by NOAA and Princeton University's Cooperative Institute for Climate Science and  
610 NASA under grants NNG14HH42I-MAP and NNH14ZDA001N-ACMAP.

611

612

613

614

615

616

617



618

## Reference

- 619 Alexander, M. A., Bladé, I., Newman, M., Lanzante, J. R., Lau, N.-C., and Scott, J. D.: The  
620 atmospheric bridge: The influence of ENSO teleconnections on air–sea interaction over  
621 the global oceans. *J. Climate*, 15, 2205–2231, 2002.
- 622 Anderson, T. L., Wu, Y., Chu, D. A., Schmid, B., Redemann, J., and Dubovik, O.: Testing the  
623 MODIS satellite retrieval of aerosol fine-mode fraction, *J. Geophys. Res.*, 110, D18204,  
624 doi: 10.1029/2005JD005978, 2005.
- 625 Banerjee, P, and Kumar, S. P.: ENSO modulation of interannual variability of dust aerosols over  
626 the northwest Indian Ocean, *J. Climate*, 29, 1287–1303, 2016.
- 627 Bangert, M., Nenes, A., Vogel, B., Vogel, H., Barahona, D., Karydis, V. A., Kumar, P.,  
628 Kottmeier, C., and Blahak, U.: Saharan dust event impacts on cloud formation and  
629 radiation over Western Europe, *Atmos. Chem. Phys.*, 12, 4045–4063, 2012.
- 630 Barlow, M., Cullen, H., and Lyon, B.: Drought in central and southwest Asia: La Niña, the  
631 warm pool, and Indian Ocean precipitation. *J. Climate*, 15, 697–700, doi:10.1175/1520-  
632 0442(2002)015,0697:DICASA.2.0.CO;2, 2002.
- 633 Chen, M., Xie, P., Janowiak, J. E. and Arkin, P. A.: Global Land Precipitation: A 50-yr Monthly  
634 Analysis Based on Gauge Observations, *J. of Hydrometeorology*, 3, 249–266, 2002.
- 635 Chin, M., et al.: Multi-decadal aerosol variations from 1980 to 2009: A perspective from  
636 observations and a global model, *Atmos. Chem. Phys.*, 14, 3657–3690, 2014.
- 637 Choobari, O. A., Zawar-Reza, P., and turman, A.: The global distribution of mineral dust and its  
638 impacts on the climate system: A review, *Atmospheric Research*, 138, 152–165, 2014.
- 639 Claverie, M., Vermote E., and NOAA CDR Program: NOAA Climate Data Record (CDR) of  
640 Leaf Area Index (LAI) and Fraction of Absorbed Photosynthetically Active Radiation



- 641 (FAPAR), Version 4. [indicate subset used]. NOAA National Climatic Data Center.  
642 doi:10.7289/V5M043BX [access date], 2014.
- 643 Claverie, M., Matthews, J. L., Vermote, E. F., and Justice, C. O.: A 30+ year AVHRR LAI and  
644 FAPAR climate data record: Algorithm description and validation, *Remote Sens.*, 8, 263;  
645 doi:10.3390/rs8030263, 2016.
- 646 Dai, A.: The influence of the inter-decadal Pacific oscillation on US precipitation during 1923-  
647 2010, *Clim. Dyn.*, 41, 633-646. doi: 10.1007/s00382-012-1446-5, 2013.
- 648 D’Almeida, G. A.: Desert aerosol characteristics and effects on climate. In *Paleoclimatology  
649 and Paleometeorology: Modern and Past patterns of Global Atmospheric Transport*.  
650 Lienen M., Sarnthein M. (eds). Kluwer Academic Publishers, 311-338, 1987.
- 651 Dayan: Climatology of back trajectories from Israel based synoptic analysis, *Journal of Climate  
652 and Applied Meteorology*, 25, 591-595, 1986.
- 653 Dayan, U., Ziv, B., Shoob, T., and Enzel, Y. : Suspended dust over southeastern Mediterranean  
654 and its relation to atmospheric circulations, *Int. J. of Climatol.*, 28, 915-924, 2008.
- 655 Dayan, U., Tubi, A., and Levy, I.: On the importance of synoptic classification methods with  
656 respect to environmental phenomena, *Int. J. of Climatol.*, 32, 681-694, 2012.
- 657 Dee, D. P. et al.: The ERA-Interim reanalysis: configuration and performance of the data  
658 assimilation system, *Q.J.R. Meteorol. Soc.*, Vol. 137: 553-597, DOI: 10.1002/qj.828,  
659 2011
- 660 Dempsey, M. J.: Forecasting strategies for Haboobs: an underreported weather phenomenon,  
661 *Advances in Meteorology*, <http://dx.doi.org/10.1155/2014/904759>, 2014.
- 662 Deser, C., and Blackmon, M. L.: On the relationship between tropical and North Pacific sea  
663 surface temperature variations. *J. Climate*, 8, 1677–1680, 1995.



- 664 Donner, L., Wyman, B. L., Hemler, R. S. and et al.: The dynamical core, physical  
665 parameterizations, and basic simulation characteristics of the atmospheric component  
666 AM3 of the GFDL global coupled model CM3, *J. Climate*, 24, 3484-3519, 2011.
- 667 Eck, T. F., Holben, B. N., Reid, J. S., Dubovik, O., Smirnov, A., O'Neill, N. T., Slutsker, I.,  
668 Kinne, S.: Wavelength dependence of the optical depth of biomass burning, urban, and  
669 desert dust aerosols, *J. Geophys. Res.*, 104(D24), 31333-31349, 1999.
- 670 Evans, M. N., Cane, M. A., Schrag, D. P., Kaplan, A., Linsley, B. K., Villalba, R., and  
671 Wellington, G. M.: Support for tropically-driven Pacific decadal variability based on  
672 paleoproxy evidence, *Geophys. Res. Lett.*, 28, 3689-3691, 2001.
- 673 Fung, I., Meyn, S., Tegen, I., Doney, S. C., John, J., and Bishop, J. K. B.: Iron supply and  
674 demand in the upper ocean, *Global Biogeochem. Cycle*, 14, 281-296, 2000.
- 675 Ginoux, P., Chin, M., Tegen, I., Prospero, J. M., Holben, B., Dubovik, O., and Lin, S.-J.: Sources  
676 and distributions of dust aerosols simulated with the GOCART model. *J. Geophys. Res.*,  
677 106, 22 255-22 274, 2001.
- 678 Ginoux, P., Prospero, J. M., Gill, T. E., Hsu, N. C., and Zhao, M.: Global-scale attribution of  
679 anthropogenic and natural dust sources and their emission rates based on the MODIS  
680 Deep Blue aerosol products, *Rev. Geophys.*, 50, RG3005, 2012.
- 681 Ginoux, P., Prospero, J. M., Torres, O., and Chin, M.: Long-term simulation of global dust  
682 distribution with the GOCART model: Correlation with North Atlantic Oscillation,  
683 *Environ. Model. Software*, 19, 113-128, doi:10.1016/S1364-8152(03)00114-2, 2004.
- 684 Harris, I., Jones, P.D., Osborn, T.J. and Lister, D.H.: Updated high-resolution grids of monthly  
685 climatic observations –the CRU TS3.10 Dataset. *Int. J. Climatol.*, 34:623-642.  
686 doi:10.1002/joc.3711, 2014.



- 687 Hsu, N. C., Tsay, S.-C., King, M., and Herman, J. R.: Aerosol properties over bright-reflecting  
688 source regions, *IEEE Trans. Geosci. Remote Sens.*, 42, 577-569, 2004.
- 689 Hsu, N. C., Tsay, S.-C. , King, M., and Herman, J. R.: Deep blue retrievals of Asian aerosol  
690 properties during ACE-Asia, *IEEE Trans. Geosci. Remote Sens.*, 44, 3180-3195, 2006.
- 691 Huang, B., Banzon, V.F., Freeman, E., Lawrimore, J., Liu, W., Peterson, T.C., Smith, T.M.,  
692 Thorne, P.W., Woodruff, S.D., and Zhang, H.-M.: Extended Reconstructed Sea Surface  
693 Temperature version 4 (ERSST.v4): Part I. Upgrades and intercomparisons. *Journal of*  
694 *Climate*, 28, 911-930, doi:10.1175/JCLI-D-14-00006.1, 2015.
- 695 Huang, B., Thorne, P., Smith, T., Liu, W., Lawrimore, J., Banzon, V., Zhang, H., Peterson, T.,  
696 and Menne, M.: Further Exploring and Quantifying Uncertainties for Extended  
697 Reconstructed Sea Surface Temperature (ERSST) Version 4 (v4). *Journal of Climate*, 29,  
698 3119-3142, doi:10.1175/JCLI-D-15-0430.1, 2016.
- 699 Huang, J., Wang, T., Wang, W., Li, Z., and Yan, H.: Climate effects of dust aerosol over East  
700 Asian arid and semiarid regions, *J. Geophys. Res. Atmos.*, 119, 11,398-11,416,  
701 doi:10.1002/2014JD21796, 2014.
- 702 Huffman, G. J., and Bolvin, D.T.: TRMM and other data precipitation data set documentation.  
703 TRMM Doc., 42 pp. [Available online at [ftp:// meso-a.gsfc.nasa.gov/pub/](ftp://meso-a.gsfc.nasa.gov/pub/trmmdocs/3B42_3B43_doc.pdf)  
704 [trmmdocs/3B42\\_3B43\\_doc.pdf](ftp://meso-a.gsfc.nasa.gov/pub/trmmdocs/3B42_3B43_doc.pdf)], 2014
- 705 Israelevich, P. L., Ganor, E., Levin, Z., and Joseph, J. H.: Annual variations of physical  
706 properties of desert dust over Israel, *J. Geophys. Res.*, 180(D13), 4381, doi:  
707 10.1029/2002JD003163, 2003.
- 708 Jin, Q., Wei, J., and Yang, Z.-L.: Positive response of indian summer rainfall to middle east dust,  
709 *Geophys. Res. Lett.*, 41 (11), 4068–4074, doi:10.1002/2014gl059980, 2014.



- 710 Jin, Q., Wei, J., Yang, Z.-L., Pu, B., and Huang, J.-P.: Consistent response of Indian summer  
711 monsoon to middle east dust in observations and simulations, *Atmospheric Chemistry  
712 and Physics*, 15 (17), 9897–9915, doi:10.5194/acp-15-9897-2015, 2015.
- 713 Jin, Q., Yang, Z.-L., and Wei, J.: Seasonal Responses of Indian Summer Monsoon to Dust  
714 Aerosols in the Middle East, India, and China. *J. Climate*. doi:10.1175/JCLI-D-15-  
715 0622.1, in press, 2016.
- 716 Kalnay, E., et al.: The NCEP/NCAR 40-year reanalysis project, *Bull. Am. Meteorol. Soc.*, 77(3),  
717 437–471, doi:10.1175/1520-0477(1996)077<0437:Tnyrp>2.0.Co;2, 1996.
- 718 Kim, M.-K., Lau, W. K. M., Kim, K.-M., Sang, J., Kim, Y.-H., and Lee, W.-S.: Amplification of  
719 ENSO effects on Indian summer monsoon by absorbing aerosols, *Clim. Dyn.*, 46, 2657-  
720 2671, 2016.
- 721 Klingmüller, K., Pozzer, A., Metzger, S., Stenchikov, G., and Lelieveld, J.: Aerosol optical depth  
722 trend over the Middle East, *Atmos. Chem. Phys.*, 16, 5063-5073, 2016.
- 723 Kubilay, N., Nickovic, S., Moulin, C., and Dulac, F.: An illustration of the transport and  
724 deposition of mineral dust onto the eastern Mediterranean. *Atmos. Environ.*, 34, 1293–  
725 1303, doi:10.1016/S1352-2310(99)00179-X, 2000.
- 726 Lau, K. M., Kim, K. M., Sud, Y. C., and Walker, G. K.: AGCM study of the response of the  
727 atmospheric water cycle of West Africa and the Atlantic to Saharan dust radiative  
728 forcing. *Ann. Geophys.*, 27, 4023–4037, doi:10.5194/angeo-27-4023-2009, 2009.
- 729 Levin, Z., Ganor, E., and Gladstein, V.: The effects of desert particles coated with sulfate on rain  
730 formation in the eastern Mediterranean. *J. Appl. Meteor.*, 35, 1511–1523, doi:10.1175/  
731 1520-0450(1996)035,1511:TEODPC.2.0.CO;2, 1996.



- 732 Li, F., Ginoux, P., and Ramaswamy, V.: Distribution, transport, and deposition of mineral dust in  
733 the Southern Ocean and Antarctica: Contribution of major sources, *J. Geophys. Res.*,  
734 113: D10207, doi:10.1029/2007JD009190, 2008.
- 735 Lin, S.-J.: A finite-volume integration method for computing pressure-gradient force in general  
736 vertical coordinates. *Quart. J. Roy. Meteor. Soc.*, 123, 1749–1762, 1997.
- 737 Lin, S.-J.: A “vertically Lagrangian” finite-volume dynamical core for global models. *Mon.*  
738 *Wea. Rev.*, 132, 2293–2307, 2004.
- 739 Lin, S.-J., , and Rood, R. B.: Multidimensional flux-form semi- Lagrangian transport schemes.  
740 *Mon. Wea. Rev.*, 124, 2046–2070, 1996.
- 741 Lin, S.-J., and Rood, R. B.: An explicit flux-form semi-Lagrangian shallow water model on the  
742 sphere. *Quart. J. Roy. Meteor. Soc.*, 123, 2477–2498, 1997.
- 743 Liu, Z., and Alexander, M.: Atmospheric bridge, oceanic tunnel, and global climatic  
744 teleconnections. *Rev. Geophys.*, 45, RG2005, doi:10.1029/2005RG000172, 2007.
- 745 Liu, W., Huang, B., Thorne, P.W., Banzon, V.F., Zhang, H.-M., Freeman, E., Lawrimore, J.,  
746 Peterson, T.C., Smith, T.M., and Woodruff, S.D.: Extended Reconstructed Sea Surface  
747 Temperature version 4 (ERSST.v4): Part II. Parametric and structural uncertainty  
748 estimations. *Journal of Climate*, 28, 931-951, doi:10.1175/JCLI-D-14-00007.1, 2015.
- 749 Mahowald, N. M., and Coauthors: Observed 20th century desert dust variability: Impact on  
750 climate and biogeochemistry. *Atmos. Chem. Phys.*, 10, 10 875–10 893, doi:10.5194/acp-  
751 10-10875-2010, 2010.
- 752 Mantua, H., and Hare, S. R.: The Pacific Decadal Oscillation, *J. of Oceanography*, 58, 35-44,  
753 2002.



- 754 Mariotti, A.: How ENSO impacts precipitation in southwest central Asia. *Geophys. Res. Lett.*,  
755 34, L16706, doi:10.1029/2007GL030078, 2007.
- 756 Mariotti, A., Ballabrera-Poy, J., and Zeng, N.: Tropical influence on Euro-Asian autumn rainfall  
757 variability. *Climate Dyn.*, 24, 511–521, doi:10.1007/s00382-004-0498-6, 2005.
- 758 Miller, R. L., and Tegen, I.: Climate response to soil dust aerosols. *J. Climate*, 11, 3247–3267,  
759 doi:10.1175/1520-0442(1998)011,3247: CRTSDA.2.0.CO;2, 1998.
- 760 Miller, R. L., Tegen, I., and Perlwitz, J.: Surface radiative forcing by soil dust aerosols and the  
761 hydrologic cycle. *J. Geophys. Res.*, 109, D04203, doi:10.1029/2003JD004085, 2004.
- 762 Miller, S., Kuciauskas, A. P., Liu, M., Ji, Q., Reid, J.S., Breed, D. W. , Walker, A. L., and  
763 Mandoos, A. A.: Haboob dust storms of the southern Arabian Peninsula, *J. Geophys.*  
764 *Res.*, 113, D01202, doi:10.1029/2007JD008550, 2008.
- 765 Mills, C. M., and Walsh, J. E.: Seasonal variation and spatial patterns of the atmospheric  
766 component of the Pacific decadal oscillation, *J. Climate*, 26, 1575-1594, 2013.
- 767 Minobe, S.: A 50-70 year climate oscillation over the North Pacific and North America,  
768 *Geophys. Res. Lett.*, 24, 683-686, 1997.
- 769 Moorthi, S. and Suarez, M. J.: Relaxed Arakawa-Schubert. A parameterization on moist  
770 convection for general circulation models, *Mon. Weather Rev.*, 120, 978-1002, 1992.
- 771 Morman, S. A., and Plumlee, G. S.: The role of airborne mineral dusts in human disease, *Aeolian*  
772 *Research*, 9, 203-212, 2013.
- 773 Moulin, C., Lambert, C. E., Dulac, F., Dayan, U.: Control of atmospheric export of dust from  
774 North Africa by the North Atlantic oscillation. *Nature*, 387, 691-694, 1997.



- 775 Nakajima, T., Higurashi, A., Kawamoto, K., and Penner, J. E.: A possible correlation between  
776 satellite-derived cloud and aerosol microphysical parameters, *Geophys. Res. Lett.*, 28,  
777 1171–1174, doi:10.1029/2000GL012186, 2001.
- 778 Newman, M., Compo, G. P. and Alexander, M.: ENSO-forced variability of the Pacific decadal  
779 oscillation, *J. Climate*, 16, 3853–3857, 2003.
- 780 Notaro, M., Alkolibi, F., Fadda, E., and Bakhrjy, F.: Trajectory analysis of Saudi Arabian dust  
781 storms, *J. Geophys. Res. Atmos.*, 118, 6028–6043. Notaro, M., Yu, Y., and O. V.  
782 Kalashnikova (2015), Regime shift in Arabian dust activity, triggered by persistent  
783 Fertile Crescent drought, *J. Geophys. Res. Atmos.*, 120, 10,229–10,249,  
784 doi:10.1002/2015JD023855, 2013.
- 785 Pozzer, A., de Meij, A., Yoon, J., Tost, H., Georgoulias, A. K., and Astitha, M.: AOD trends  
786 during 2001–2010 from observations and model simulations, *Atmos. Chem. Phys.*, 15,  
787 5521–5535, 2015. doi:10.5194/acp-15-5521-2015.
- 788 Price, C., Stone, L., Huppert, A., Rajagopalan, B., and Alpert, P.: A possible link between El  
789 Niño and precipitation in Israel, *Geophys. Res. Lett.*, 25, 3963–3966,  
790 doi:10.1029/1998GL900098, 1998.
- 791 Rayner, N. A., Parker, D. E., Horton, E. B., Folland, C. K., Alexander, L. V., Rowell, D. P.,  
792 Kent, E. C., Kaplan, A.: Global analyses of sea surface temperature, sea ice, and night  
793 marine air temperature since the late nineteenth century *J. Geophys. Res.* Vol. 108, No.  
794 D14, 4407 10.1029/2002JD002670, 2003.
- 795 Roberts, A., and Knippertz, P.: Haboobs: convectively generated dust storms in West Africa,  
796 *Weather*, 67, 311–316, 2012.



- 797 Rosenfeld, J. E., Considine, D. B., Meade, P. E., Bacmeister, J. T., Jackman, C. H., and  
798 Schoeberl, M. R.: Stratospheric effects of Mount Pinatubo aerosol studied with a coupled  
799 two-dimensional model, *J. Geophys. Res.*, 102, 3649–3670, doi:10.1029/96JD03820,  
800 1997.
- 801 Schneider, N., and Cornuelle, B.: The forcing of the Pacific decadal oscillation, *J. Climate*, 18,  
802 4355-4373, 2005.
- 803 Shao, Y.: A model for mineral dust emission, *J. Geophys. Res.*, 160(D17), 20, 239-  
804 20,254,doi:10.1029/2001JD900171, 2001.
- 805 Shao, Y., Wyrwoll, K. H., and Cappell, A., et al.: Dust cycle: an emerging core theme in Earth  
806 system science. *Aeolian Res.*, 2, 181-204, 2011.
- 807 Simmons, A. J., and Burridge, D. M.: An energy and angular momentum conserving vertical  
808 finite-difference scheme and hybrid vertical coordinates. *Mon. Wea. Rev.*, 109, 758–766,  
809 1981.
- 810 Solomon, F., Mallet, M., Elguindi, N., Fiorfi, F., Zakey, A., and Konare, A. : Dust aerosol impact  
811 on regional precipitation over western Africa, mechanisms and sensitivity to absorption  
812 properties. *Geophys. Res. Lett.*, 35, L24705, doi:10.1029/2008GL035900, 2008.
- 813 Solomon, F., Elguindi, N., and Mallet, M.: Radiative and climatic effects of dust over West  
814 Africa, as simulated by a regional climate model. *Climate Res.*, 52, 97–113,  
815 doi:10.3354/cr01039, 2012.
- 816 Solomon, F., Nair, V. S., and Mallet, M.: Increasing Arabian dust activity and the Indian summer  
817 monsoon, *Atmos. Chem. Phys.*, 15, 8051–8064, doi:10.5194/acp-15-8051-2015, 2015.
- 818 Strong, C., and Magnusdottir, G.: The role of tropospheric Rossby wave breaking in the Pacific  
819 decadal oscillation, 22, 1819-1833, 2009.



- 820 Strong, J. D.O., Vecchi, G. A., and Ginoux, P.: The response of the tropical Atlantic and West  
821 African climate to Saharan dust in a fully coupled GCM, *J. climate*, 28, 7071-7092, 2015.
- 822 Tegen, I., Lacis, A., and Fung, I.: The influence of mineral aerosol from disturbed soils on the  
823 global radiation budget, *Nature*, 380, 419-422, 1996.
- 824 Vinoj, V., Rasch, P. J., Wang, H. L., Yoon, J. H., Ma, P. L., Landu, K., and Singh, B.: Short-  
825 term modulation of Indian summer monsoon rainfall by West Asian dust, *Nat. Geosci.*, 7,  
826 308–313, 2014.
- 827 Vukovi, A., Vujadinovic, M., Pejanovic, G., Andric, J., Kumjian, M. R., Djurdjevic, V., Dacic,  
828 M., Prasad, A. K., El-Askary, H. M., Paris, B. C., Petkovic, S., Nickovic, S., and Sprigg,  
829 W. A.: Numerical simulation of “an American haboob”, *Atmos. Chem. Phys.*, 14, 3211-  
830 3230, 2014.
- 831 Wang, S., Huang, J., He, Y., and Guan, Y.: Combined effects of the Pacific Decadal Oscillation  
832 and El Niño-Southern Oscillation on global land dry-wet changes, *Sci. Rep.*, 4, 6651,  
833 doi:10.1038/srep06651, 2014.
- 834 Wurzler, S. C., Reisin, T. G., and Levin, Z.: Modification of mineral dust particles by cloud  
835 processing and subsequent effects on drop size distributions, *J. Geophys. Res.*, 105(D4),  
836 4501–4512, doi:10.1029/1999JD900980, 2000.
- 837 Yoshioka, M., Mahowald, N. M., Conley, A. J., Collins, W. D., Fillmore, D. W., Zender, C. S.,  
838 and Coleman, D. B.: Impact of desert dust radiative forcing on Sahel precipitation:  
839 Relative importance of dust compared to sea surface temperature variations, vegetation  
840 changes, and greenhouse gas warming. *J. Climate*, 20, 1445–1467,  
841 doi:10.1175/JCLI4056.1, 2007.



842 Yu, Y., Notaro, M., Liu, Z., Wang, F., Alkolibi, F., Fadda, E., and Bakhrjy, F.: Climatic controls  
843 on the interannual to decadal variability in Saudi Arabian dust activity: Toward the  
844 development of a seasonal dust prediction model, *J. Geophys. Res. Atmos.*, 120, 1739–  
845 1758, 2015.

846 Yue, X., Wang, H., Liao, H., and Fan, K.: Direct climatic effect of dust aerosol in the NCAR  
847 Community Atmosphere Model version 3 (CAM3). *Adv. Atmos. Sci.*, 27, 230–242,  
848 doi:10.1007/s00376-009-8170-z, 2010.

849 Yue, X., Liao, H., Wang, H. J., Li, S. L., and Tang, J. P.: Role of sea surface temperature  
850 responses in simulation of the climatic effect of mineral dust aerosol. *Atmos. Chem.*  
851 *Phys.*, 11, 6049–6062, doi:10.5194/acp-11-6049-2011, 2011.

852 Zhang, Y., Wallace, J. M., and Battisti, D. S.: ENSO-like interdecadal variability, *J. Clim.*, 10,  
853 1004–1020. Zhang, L., And T. Delworth, 2015: Analysis of the characteristic and  
854 mechanisms of the Pacific decadal oscillation in a suite of coupled models from the  
855 Geophysical Fluid Dynamics Laboratory, *J. Climate*, 28, 7678-7701, 1997.

856

857

858

859

860

861

862

863

864



865 Table 1 Correlations between monthly DOD indices and the PDO, Niño3.4 indices, precipitation from the  
866 CRU TS3.23 (P1; 2003-2014) and PRECL (P2), AVHRR LAI (LAI1), MODIS Aqua LAI (LAI2) and 10  
867 m wind speed from the ERA-Interim averaged over Syria (see the box in Fig.2) for all the month  
868 (seasonal cycles are removed) from 2003-2015 (or 2014). Coefficients significant at the 95% confidence  
869 level are in bold.

870

871 Table 2 Same as table 1 but for MAM average from 2003-2015 (or 2014). Coefficients significant at the  
872 95% confidence level are in bold.

873

874

875

876

877

878

879

880

881

882

883

884

885

886

887

888

889

890



891 Figure 1. Monthly time series of Aqua (green) and Terra (grey) DOD indices averaged over Syria (see  
892 Fig. 2 for domain) and PDO index (orange; multiplying by -1 to show its negative connection with the  
893 DOD indices).

894

895 Figure 2. Correlation between the PDO index and MODIS (a) Aqua and (b) Terra DOD in MAM from  
896 2003-2015. (c) Correlation between Syrian DOD indices (navy and green bar denotes Terra and Aqua,  
897 respectively) and PDO index for each month and annual mean (ANN) from 2003 to 2015. Red dashed  
898 lines denote the 95% confidence level (t test). Red box denotes the averaging area for Syrian DOD index.

899

900 Figure 3. Correlation between the PDO index and HadISST (over the ocean) and CRU TS3.23 near-  
901 surface temperature (over land) for (a) MAM and (b) annual mean during 2003-2014. Correlation  
902 between (c)-(d) Aqua and (e)-(f) Terra DOD indices and HadISST and CRU near-surface temperature for  
903 (c), (e) MAM and (d), (f) annual mean during 2003-2014. Areas significant at the 95% confidence level  
904 (t-test) are dotted.

905

906 Figure 4. Regression of 850 hPa (shading) and 200 hPa (blue contours; solid lines for positive values and  
907 dashed lines for negative values, from -40 gpm to 40 gpm with an interval of 10 gpm, zero line is not  
908 shown) geopotential heights onto the standardized PDO index for (a) 2003-2015 and (c) 1948-2015 and  
909 onto the standardized (b) Aqua and (d) Terra DOD indices. Areas significant at the 95% confidence level  
910 (t-test) are dotted.

911

912 Figure 5. Regressions of NCEP1 850 hPa geopotential height (shading; gpm) and horizontal winds  
913 (vectors;  $\text{m s}^{-1}$ ) onto the standardized PDO index during (a) 2003-2015 and (c) 1948-2015, and onto the  
914 standardized (b) Aqua and (d) Terra DOD indices during 2003-2015. Area where the regression is  
915 significant at the 95% confidence level (t-test) is dotted, and vectors significant at the 90% confidence  
916 level are plotted in blue.



917 Figure 6. Regressions of ERA-Interim 10 meter horizontal winds (green vectors;  $\text{m s}^{-1}$ ) and cubic wind  
918 speed (shading;  $\text{m}^3 \text{s}^{-3}$ ) onto standardized PDO index (a) from 2003-2015 and (c) from 1979-2015 and  
919 onto the standardized (b) Aqua and (d) Terra DOD indices. Areas where the regressions of the wind speed  
920 are significant at the 95% confidence level are dotted and vectors significant at the 90% confidence level  
921 are plotted in blue (t-test).

922

923 Figure 7. Correlation between PRECL precipitation and PDO index during (a) 2003-2015, (c) 1948-2015  
924 and between precipitation and (b) Aqua and (d) Terra DOD indices during 2003-2015. Areas where the  
925 correlation coefficients are significant at the 95% confidence level (t-test) are dotted.

926

927 Figure 8. Regression of vertically integrated mass weighted monthly moisture flux (vectors;  $\text{kg m}^{-1} \text{s}^{-1}$ )  
928 and its magnitude (shading) onto standardized PDO index during (a) 2003-2015 and (c) 1948-2015, and  
929 onto the standardized (b) Aqua and (d) Terra DOD indices. Moisture flux is integrated from surface to  
930 300 hPa. Areas with magnitude of moisture flux significant at the 90% confidence level are dotted, and  
931 moisture fluxes significant at the 90% confidence level are plotted in purple vectors (t-test).

932

933 Figure 9. Regression of vertically integrated MSE ( $10^4 \text{ J m}^{-2}$ ) over the lowest four atmospheric layers  
934 (1000, 925, 850, and 700 hPa) from the NCEP1 onto the standardized PDO index for (a) 2003-2015 and  
935 (c) 1948-2015 and onto the standardized DOD indices from MODIS (b) Aqua and (d) Terra during 2003-  
936 2015. Areas significant at the 90% confidence level (t-test) are dotted.

937

938 Figure 10. Composites of (a) Aqua and (b) Terra daily DOD (shading) along with ERA-Interim 10 m  
939 horizontal wind anomalies (with reference to the 1979-2015 mean; vectors) for days with Syrian DOD  
940 index (Aqua) greater than 1 standard deviation during MAM from 2003-2015. Shading shows values  
941 significant at the 95% confidence level over land, while wind vectors significant at the 95% confidence  
942 are plotted in blue (t-test).



943 Figure 11. Composites of daily precipitation anomalies (shading; % with references to the climatology)  
944 from (a) the ERA-interim and (b) TRMM for the days with Syrian DOD index (Aqua) greater than 1  
945 standard deviation during MAM from 2003-2015. Areas significant at the 95% confidence level (t-test)  
946 are dotted.

947

948 Figure 12. Composites of (a) vertically integrated mass-weighted moisture flux (vectors;  $\text{kg m}^{-1}\text{s}^{-1}$ ) and its  
949 magnitude (shading) from the NCEP1 and (b) CAPE ( $10^4 \text{ J/kg}$ ) along with 850 hPa winds ( $\text{m s}^{-1}$ ) from the  
950 ERA-Interim for the days with Syrian DOD index (Aqua) greater than 1 standard deviation during MAM  
951 from 2003-2015. Moisture flux is integrated from surface to 300 hPa. Shading areas significant at the  
952 95% confidence level are dotted.

953

954 Figure 13. (a) Correlation between AM3 DOD index averaged over Syria (see Fig. 2) and surface  
955 temperature from 1960-2010 and (b) regression of 850 hPa (shading) and 200 hPa (contours; solid lines  
956 for positive values and dashed lines for negative values, from -20 gpm to 20 gpm with intervals of 5 gpm,  
957 zero line is not shown) geopotential height onto the standardized DOD index from 1960-2010. Shading  
958 areas significant at the 95% confidence level are dotted.

959

960

961

962

963

964

965

966

967

968



969 Table 1 Correlations between monthly DOD indices and the PDO, Niño3.4 indices, precipitation from the  
 970 CRU TS3.23 (P1; 2003-2014) and PRECL (P2), AVHRR LAI (LAI1), MODIS Aqua LAI (LAI2) and 10  
 971 m wind speed from the ERA-Interim averaged over Syria (see the box in Fig.2) for all the month  
 972 (seasonal cycles are removed) from 2003-2015 (or 2014). Coefficients significant at the 95% confidence  
 973 level are in bold.

	PDO	Niño3.4	P1	P2	LAI1	LAI2	10 m wind
Aqua DOD	<b>-0.51</b>	<b>-0.24</b>	-0.05	-0.05	<b>-0.35</b>	<b>-0.41</b>	-0.00
Terra DOD	<b>-0.50</b>	<b>-0.23</b>	-0.05	-0.06	<b>-0.32</b>	<b>-0.39</b>	-0.02

976

977

978

979

980

981 Table 2 Same as table 1 but for MAM average from 2003-2015 (or 2014). Coefficients significant at the  
 982 95% confidence level are in bold.

983

	PDO	Niño3.4	P1	P2	LAI1	LAI2	10 m wind
Aqua DOD	<b>-0.90</b>	<b>-0.60</b>	-0.14	-0.38	<b>-0.60</b>	<b>-0.64</b>	0.31
Terra DOD	<b>-0.90</b>	<b>-0.60</b>	-0.10	-0.34	<b>-0.57</b>	<b>-0.61</b>	0.30

984

985

986

987

988

989

990

991

992

993

994

995

996

997

998

999

1000

1001

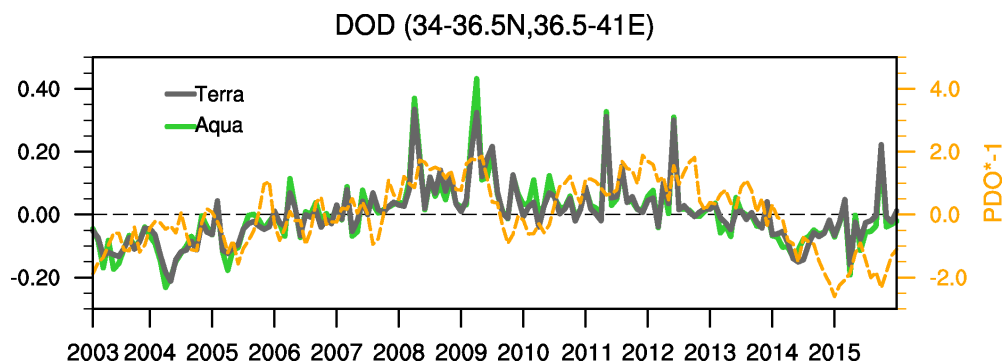
1002

1003

1004

1005

1006



1007

1008 Figure 1. Monthly time series of Aqua (green) and Terra (grey) DOD indices averaged over Syria (see  
 1009 Fig. 2 for domain) and PDO index (orange; multiplying by -1 to show its negative connection with the  
 1010 DOD indices).

1011

1012

1013

1014

1015

1016

1017

1018

1019

1020

1021

1022

1023

1024

1025

1026

1027

1028

1029

1030

1031

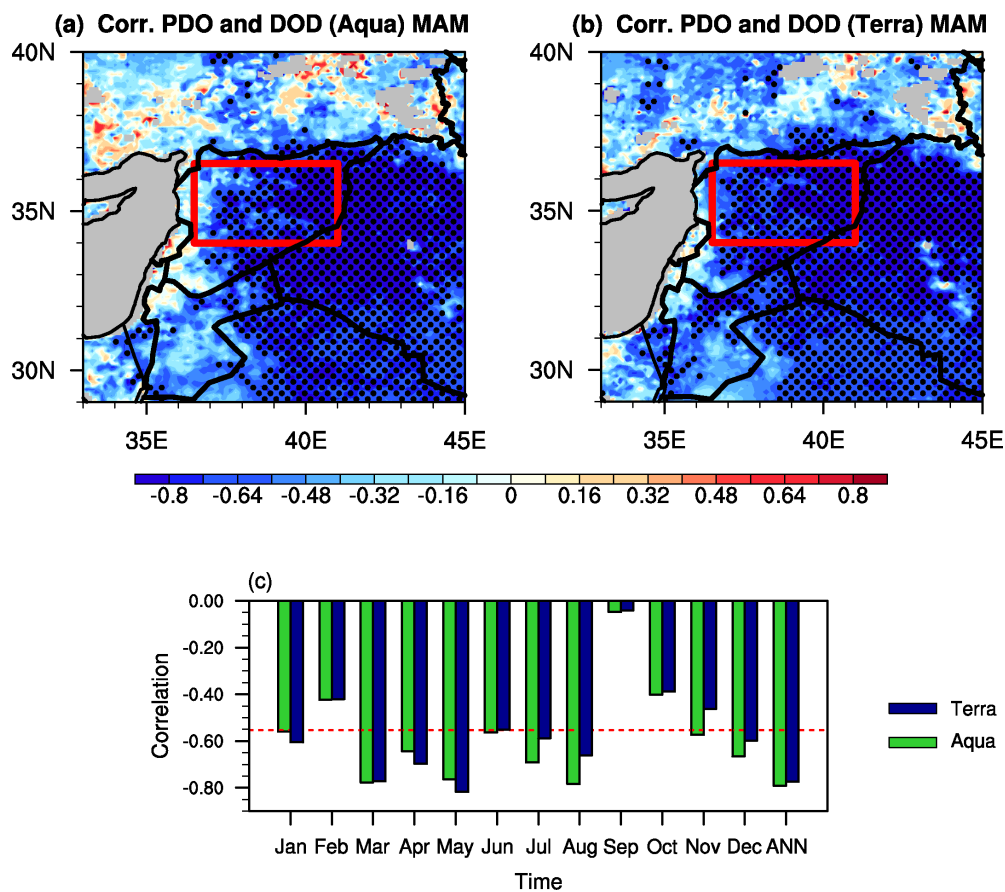
1032

1033

1034

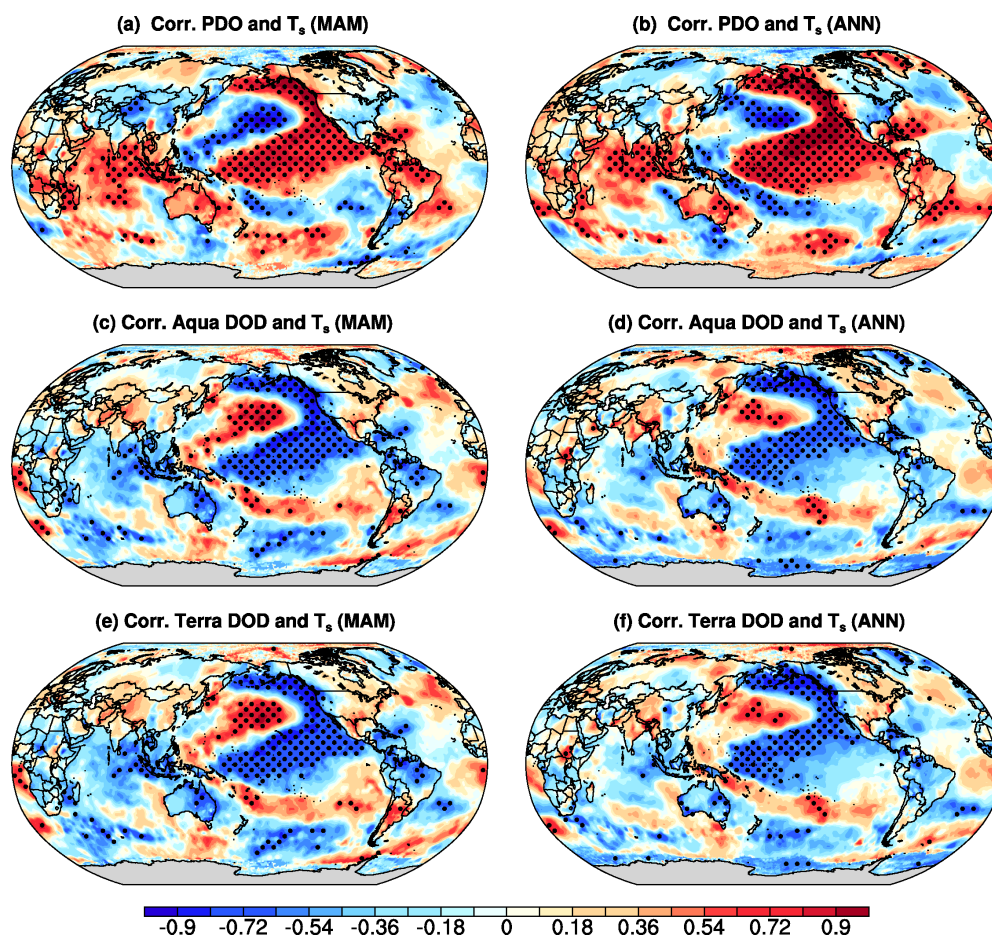
1035

1036



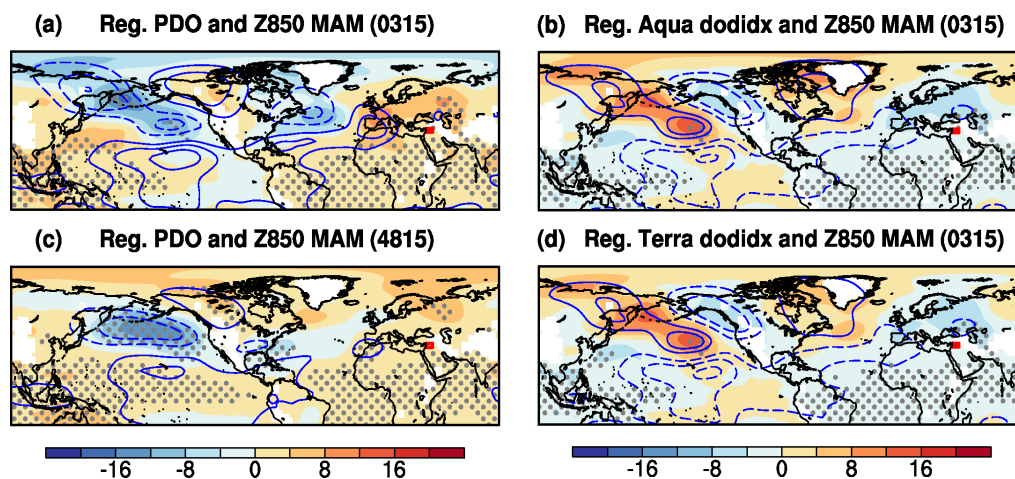
1037  
 1038 Figure 2. Correlation between the PDO index and MODIS (a) Aqua and (b) Terra DOD in MAM from  
 1039 2003-2015. (c) Correlation between Syrian DOD indices (navy and green bar denotes Terra and Aqua,  
 1040 respectively) and PDO index for each month and annual mean (ANN) from 2003 to 2015. Red dashed  
 1041 lines denote the 95% confidence level (t test). Red box denotes the averaging area for Syrian DOD index.  
 1042

1043  
 1044  
 1045  
 1046  
 1047  
 1048  
 1049  
 1050



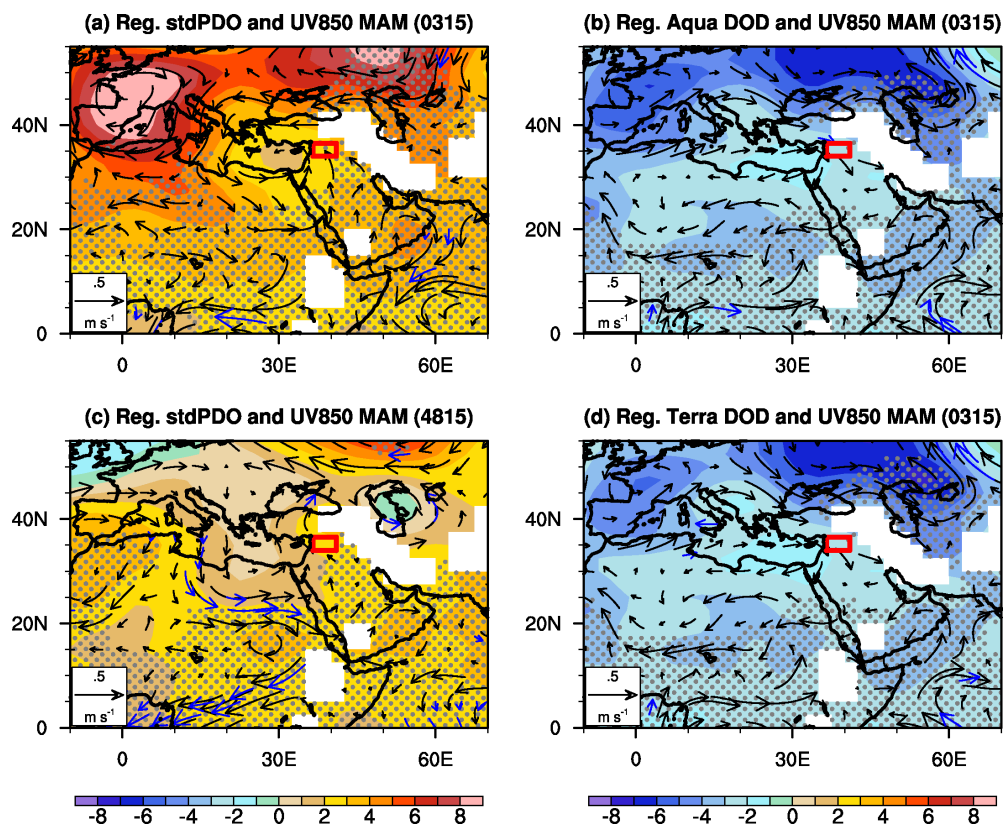
1051  
1052  
1053  
1054  
1055  
1056  
1057  
1058  
1059  
1060  
1061  
1062  
1063  
1064  
1065  
1066  
1067

Figure 3. Correlation between the PDO index and HadISST (over the ocean) and CRU TS3.23 near-surface temperature (over land) for (a) MAM and (b) annual mean during 2003-2014. Correlation between (c)-(d) Aqua and (e)-(f) Terra DOD indices and HadISST and CRU near-surface temperature for (c), (e) MAM and (d), (f) annual mean during 2003-2014. Areas significant at the 95% confidence level (t-test) are dotted.



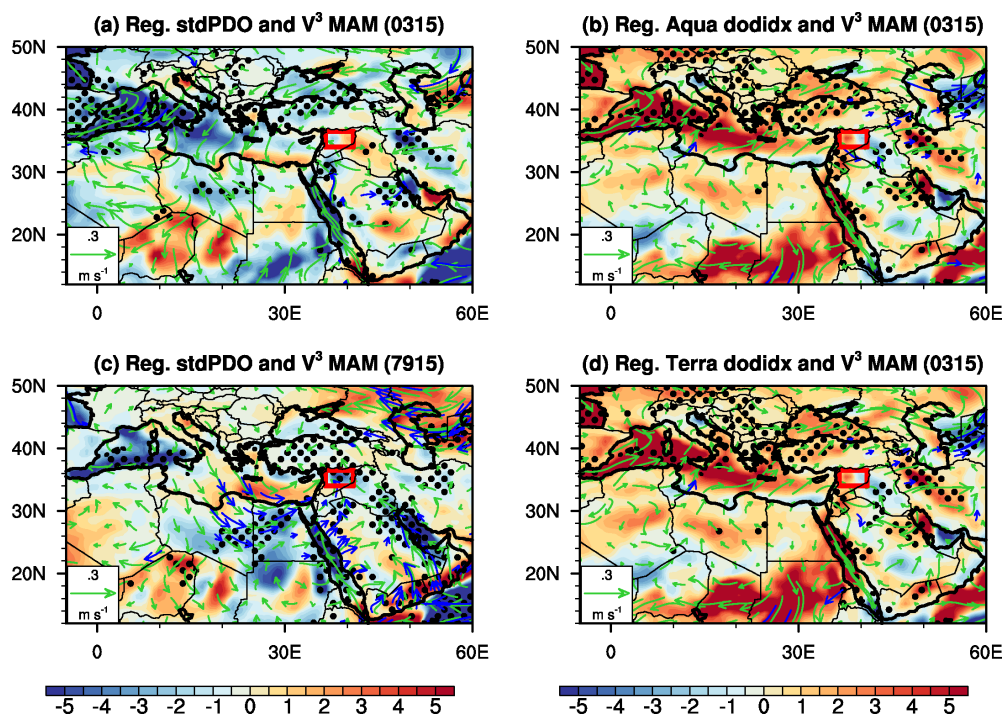
1068 Figure 4. Regression of 850 hPa (shading) and 200 hPa (blue contours; solid lines for positive values and  
1069 dashed lines for negative values, from -40 gpm to 40 gpm with an interval of 10 gpm, zero line is not  
1070 shown) geopotential heights onto the standardized PDO index for (a) 2003-2015 and (c) 1948-2015 and  
1071 onto the standardized (b) Aqua and (d) Terra DOD indices. Areas significant at the 95% confidence level  
1072 (t-test) are dotted.

1073  
1074  
1075  
1076



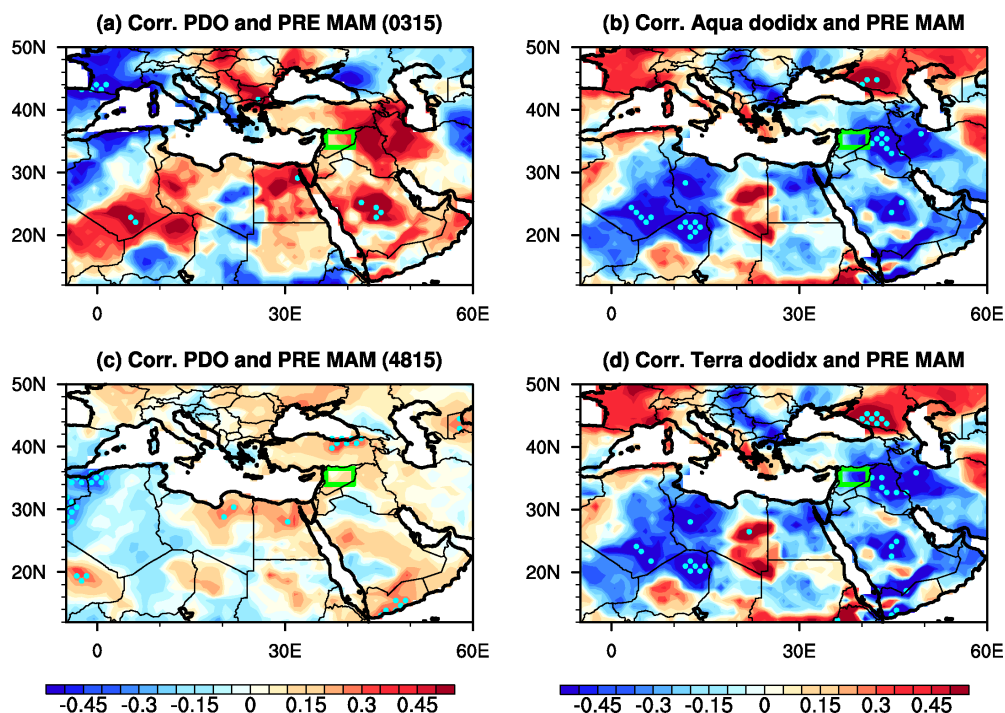
1077  
1078 Figure 5. Regressions of NCEP1 850 hPa geopotential height (shading; gpm) and horizontal winds  
1079 (vectors;  $\text{m s}^{-1}$ ) onto the standardized PDO index during (a) 2003-2015 and (c) 1948-2015, and onto the  
1080 standardized (b) Aqua and (d) Terra DOD indices during 2003-2015. Area where the regression is  
1081 significant at the 95% confidence level (t-test) is dotted, and vectors significant at the 90% confidence  
1082 level are plotted in blue.

1083  
1084  
1085  
1086  
1087  
1088  
1089  
1090  
1091  
1092  
1093  
1094  
1095  
1096



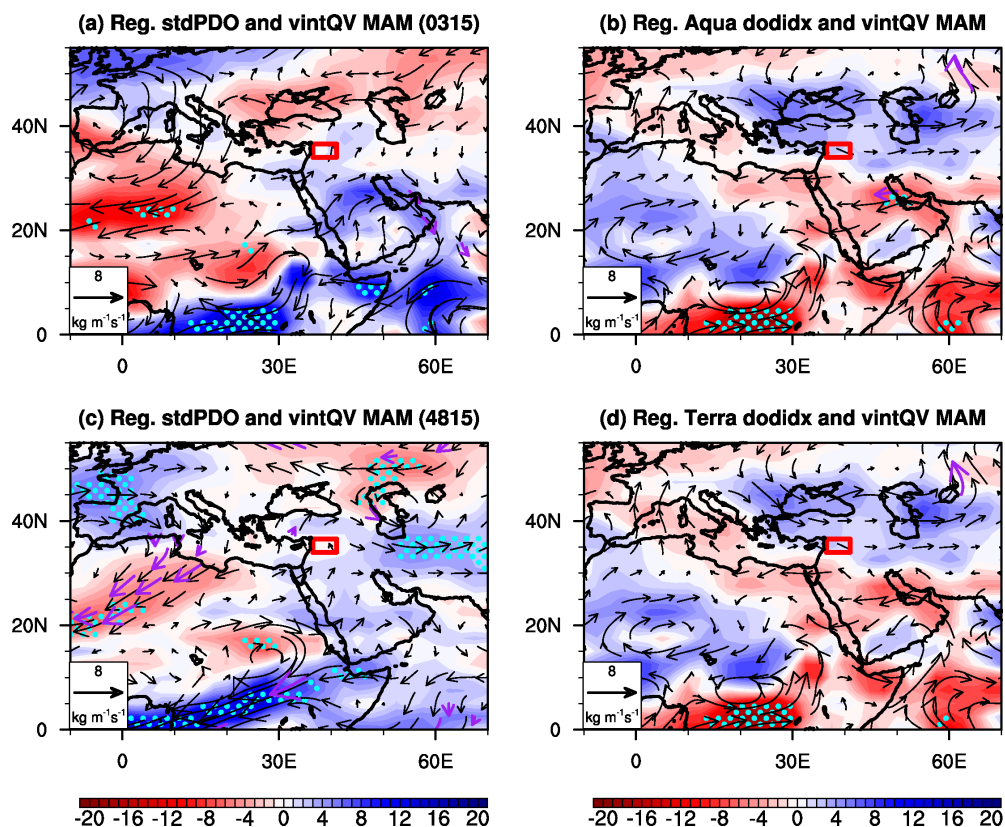
1097  
1098  
1099  
1100  
1101  
1102  
1103  
1104  
1105  
1106  
1107  
1108  
1109  
1110  
1111  
1112  
1113  
1114  
1115

Figure 6. Regressions of ERA-Interim 10 meter horizontal winds (green vectors;  $\text{m s}^{-1}$ ) and cubic wind speed (shading;  $\text{m}^3 \text{s}^{-3}$ ) onto standardized PDO index (a) from 2003-2015 and (c) from 1979-2015 and onto the standardized (b) Aqua and (d) Terra DOD indices. Areas where the regressions of the wind speed are significant at the 95% confidence level are dotted and vectors significant at the 90% confidence level are plotted in blue (t-test).



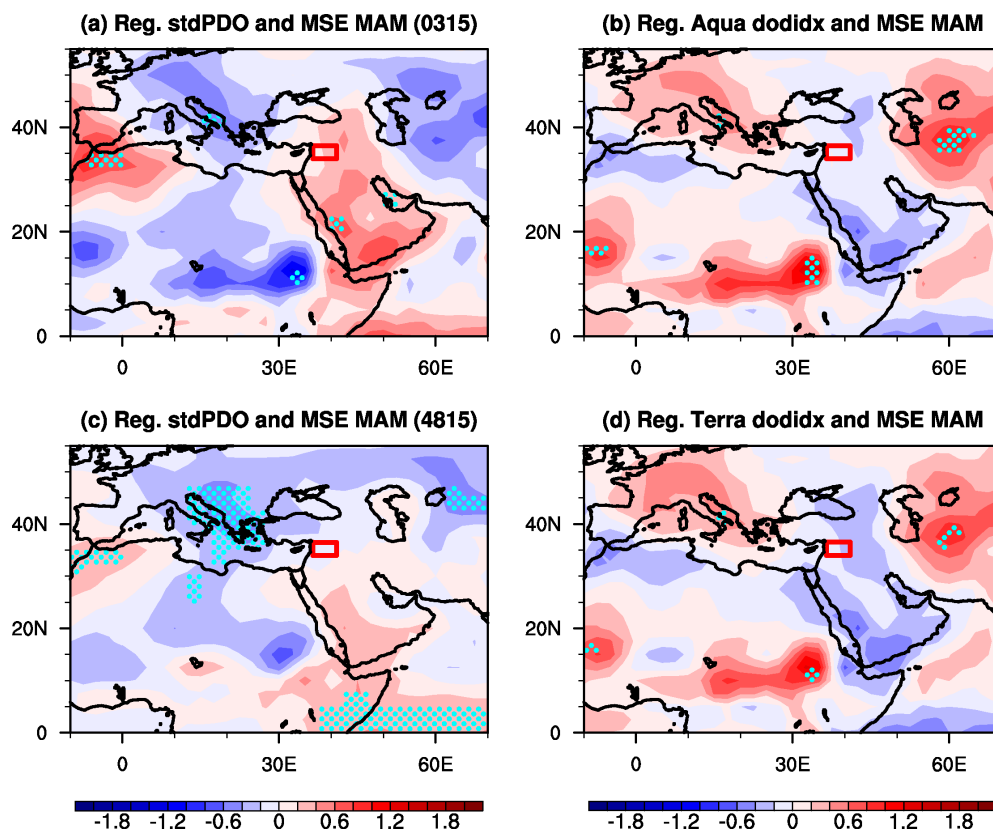
1116  
1117  
1118  
1119  
1120  
1121  
1122  
1123

Figure 7. Correlation between PRECL precipitation and PDO index during (a) 2003-2015, (c) 1948-2015 and between precipitation and (b) Aqua and (d) Terra DOD indices during 2003-2015. Areas where the correlation coefficients are significant at the 95% confidence level (t-test) are dotted.



1124  
1125 Figure 8. Regression of vertically integrated mass weighted monthly moisture flux (vectors;  $\text{kg m}^{-1} \text{s}^{-1}$ )  
1126 and its magnitude (shading) onto standardized PDO index during (a) 2003-2015 and (c) 1948-2015, and  
1127 onto the standardized (b) Aqua and (d) Terra DOD indices. Moisture flux is integrated from surface to  
1128 300 hPa. Areas with magnitude of moisture flux significant at the 90% confidence level are dotted, and  
1129 moisture fluxes significant at the 90% confidence level are plotted in purple vectors (t-test).

1130  
1131  
1132  
1133  
1134  
1135  
1136  
1137  
1138  
1139  
1140



1141

1142 Figure 9. Regression of vertically integrated MSE ( $10^4 \text{ J m}^{-2}$ ) over the lowest four atmospheric layers  
1143 (1000, 925, 850, and 700 hPa) from the NCEP1 onto the standardized PDO index for (a) 2003-2015 and  
1144 (c) 1948-2015 and onto the standardized DOD indices from MODIS (b) Aqua and (d) Terra during 2003-  
1145 2015. Areas significant at the 90% confidence level (t-test) are dotted.

1146

1147

1148

1149

1150

1151

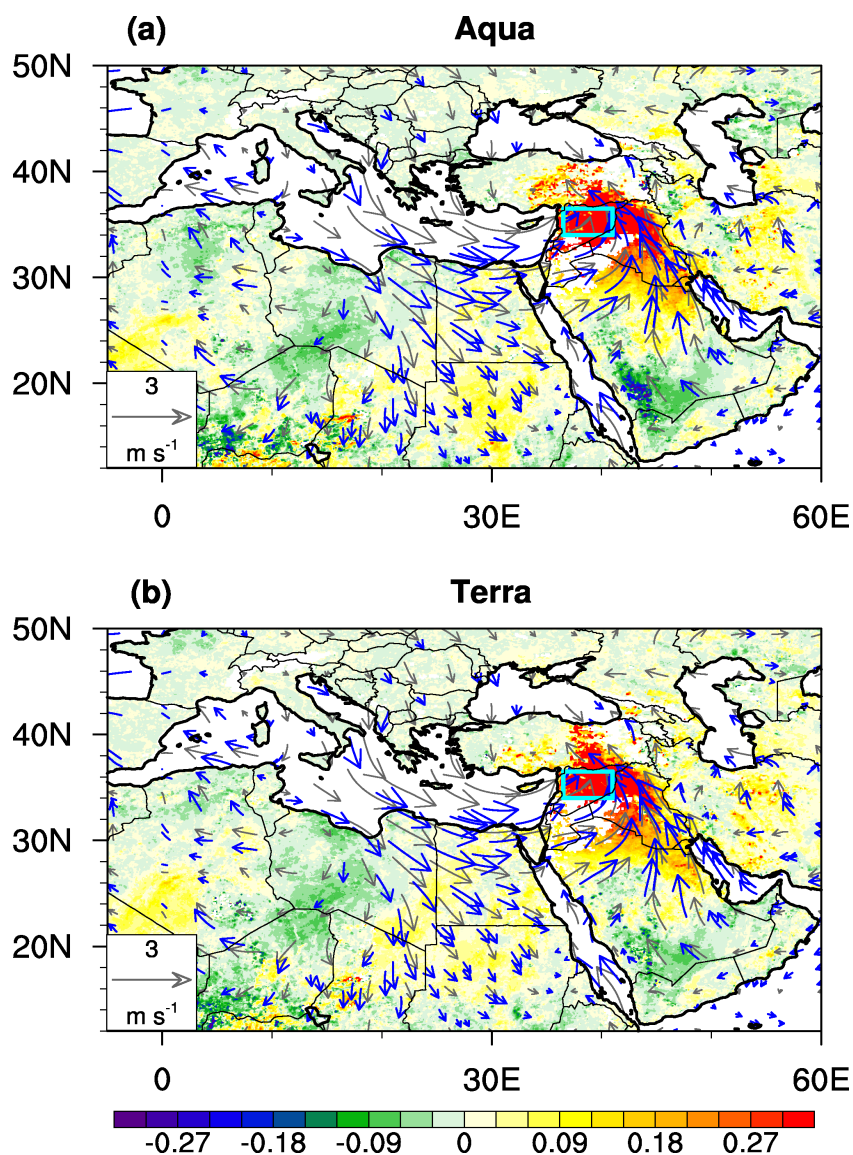
1152

1153

1154

1155

1156



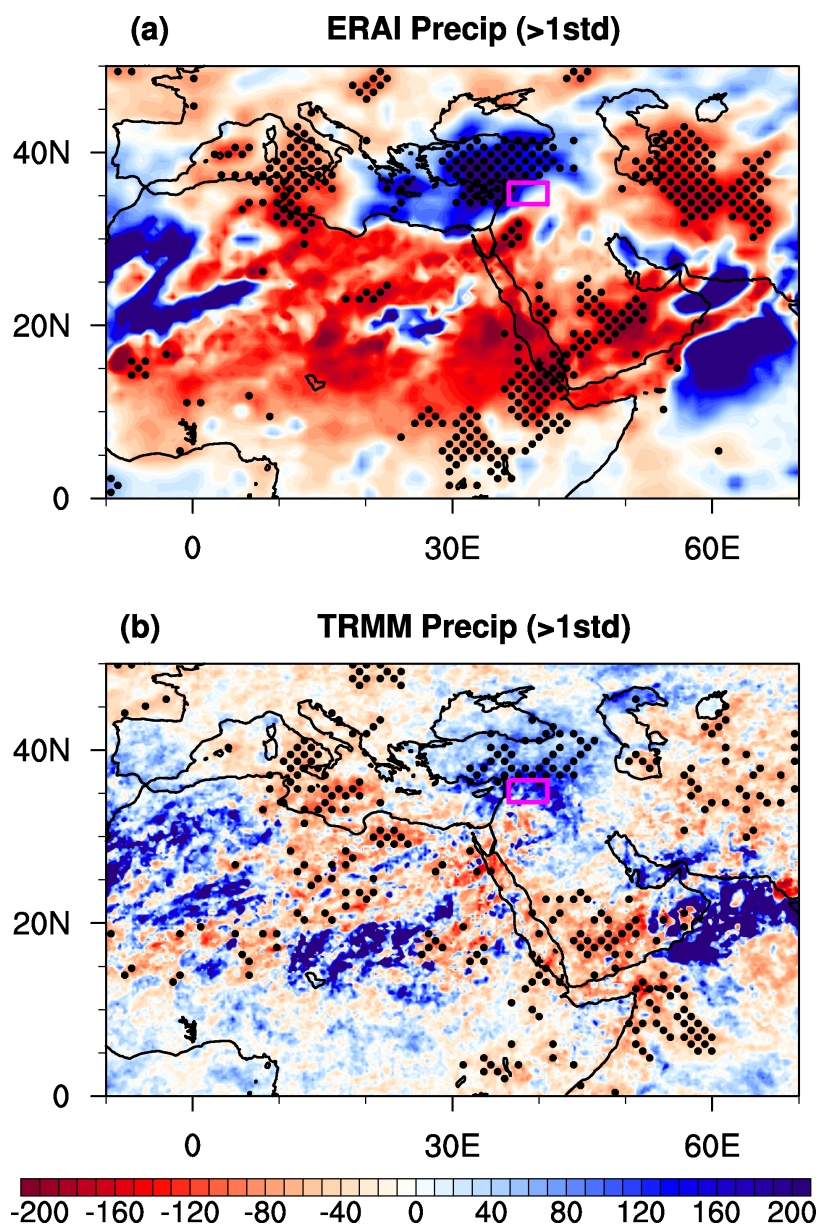
1157

1158 Figure 10. Composites of (a) Aqua and (b) Terra daily DOD (shading) along with ERA-Interim 10 m  
1159 horizontal wind anomalies (with reference to the 1979-2015 mean; vectors) for days with Syrian DOD  
1160 index (Aqua) greater than 1 standard deviation during MAM from 2003-2015. Shading shows values  
1161 significant at the 95% confidence level over land, while wind vectors significant at the 95% confidence  
1162 are plotted in blue (t-test).

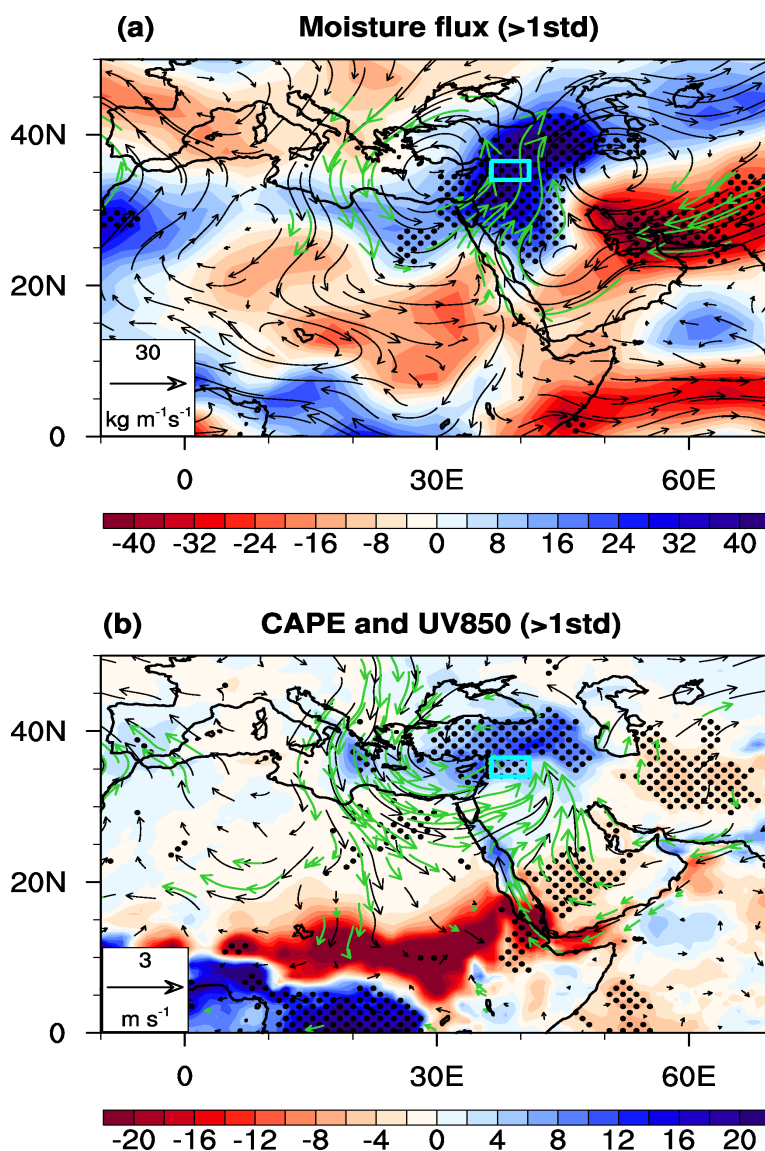
1163

1164

1165



1166  
1167 Figure 11. Composites of daily precipitation anomalies (shading; % with references to the climatology)  
1168 from (a) the ERA-interim and (b) TRMM for the days with Syrian DOD index (Aqua) greater than 1  
1169 standard deviation during MAM from 2003-2015. Areas significant at the 95% confidence level (t-test)  
1170 are dotted.  
1171  
1172  
1173

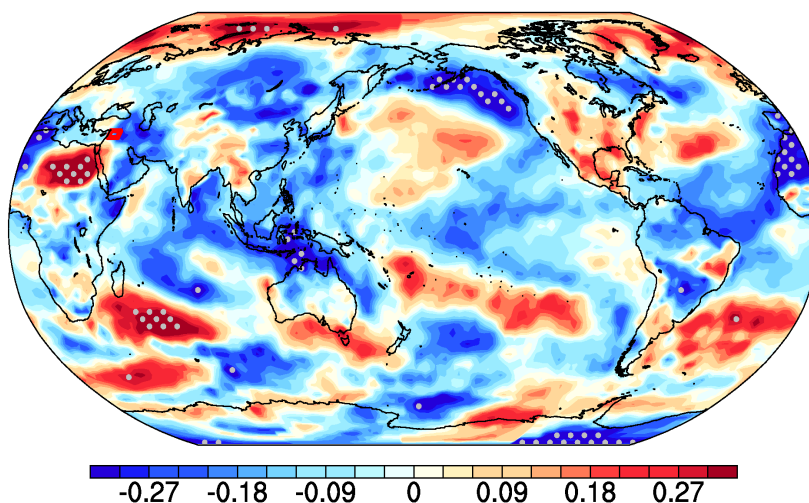


1174  
1175 Figure 12. Composites of (a) vertically integrated mass-weighted moisture flux (vectors;  $\text{kg m}^{-1}\text{s}^{-1}$ ) and  
1176 its magnitude (shading) from the NCEP1 and (b) CAPE ( $10^4 \text{ J/kg}$ ) along with 850 hPa winds ( $\text{m s}^{-1}$ ) from the  
1177 ERA-Interim for the days with Syrian DOD index (Aqua) greater than 1 standard deviation during MAM  
1178 from 2003-2015. Moisture flux is integrated from surface to 300 hPa. Shading areas significant at the  
1179 95% confidence level are dotted.  
1180  
1181  
1182

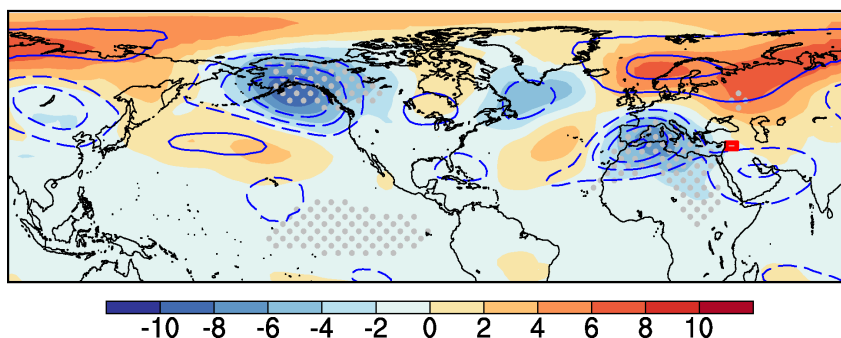


MAM (1960-2010)

(a) Corr. DODidx and Ts



(b) Reg. stdDODidx and z850



1183

1184

1185

1186

1187

1188

1189

1190

1191

Figure 13. (a) Correlation between AM3 DOD index averaged over Syria (see Fig. 2) and surface temperature from 1960-2010 and (b) regression of 850 hPa (shading) and 200 hPa (contours; solid lines for positive values and dashed lines for negative values, from -20 gpm to 20 gpm with intervals of 5 gpm, zero line is not shown) geopotential height onto the standardized DOD index from 1960-2010. Shading areas significant at the 95% confidence level are dotted.